REPORT DOCUMENTATION PAGE

1a. REPORT SECURITY CLASSIFICATION Unclassified	**1b. RESTRICTIVE MARKINGS**
2a. SECURITY CLASSIFICATION AUTHORITY	**3. DISTRIBUTION/AVAILABILITY OF REPORT** Approved for public release; distribution unlimited.
2b. DECLASSIFICATION/DOWNGRADING SCHEDULE	
4. PERFORMING ORGANIZATION REPORT NUMBER(S) 1988:4	**5. MONITORING ORGANIZATION REPORT NUMBER(S)** ESD-TR-88-250

6a. NAME OF PERFORMING ORGANIZATION Lincoln Laboratory, MIT	6b. OFFICE SYMBOL *(If applicable)*	7a. NAME OF MONITORING ORGANIZATION Electronic Systems Division

6c. ADDRESS *(City, State, and Zip Code)* P.O. Box 73 Lexington, MA 02173-0073	7b. ADDRESS *(City, State, and Zip Code)* Hanscom AFB, MA 01731

8a. NAME OF FUNDING/SPONSORING ORGANIZATION HQ AF Systems Command	8b. OFFICE SYMBOL *(If applicable)* AFSC/XTKT	9. PROCUREMENT INSTRUMENT IDENTIFICATION NUMBER F19628-85-C-0002

8c. ADDRESS *(City, State, and Zip Code)* Andrews AFB Washington, DC 20334-5000	10. SOURCE OF FUNDING NUMBERS			
	PROGRAM ELEMENT NO. 63250F	PROJECT NO. 649L	TASK NO.	WORK UNIT ACCESSION NO.

11. TITLE *(Include Security Classification)*

Solid State Research

12. PERSONAL AUTHOR(S)
Alan L. McWhorter

13a. TYPE OF REPORT Quarterly Technical Report	13b. TIME COVERED FROM 8/1/88 TO 10/31/88	14. DATE OF REPORT *(Year, Month, Day)* 1988, November, 15	15. PAGE COUNT 88

16. SUPPLEMENTARY NOTATION

None

17. COSATI CODES			18. SUBJECT TERMS *(Continue on reverse if necessary and identify by block number)*
FIELD	GROUP	SUB-GROUP	electrooptical devices analog device technology microwave semiconductor quantum electronics lasers devices materials research optical modulators charge-coupled devices submicrometer technology silicon-on-insulator films quantum-well devices microelectronics laser photoprocessing superconductors

19. ABSTRACT *(Continue on reverse if necessary and identify by block number)*

This report covers in detail the research work of the Solid State Division at Lincoln Laboratory for the period 1 August through 31 October 1988. The topics covered are Electrooptical Devices, Quantum Electronics, Materials Research, Submicrometer Technology, Microelectronics, and Analog Device Technology. Funding is provided primarily by the Air Force, with additional support provided by the Army, DARPA, Navy, SDIO, NASA, and DOE.

20. DISTRIBUTION/AVAILABILITY OF ABSTRACT ☐ UNCLASSIFIED/UNLIMITED ☒ SAME AS RPT. ☐ DTIC USERS	21. ABSTRACT SECURITY CLASSIFICATION Unclassified	
22a. NAME OF RESPONSIBLE INDIVIDUAL Lt. Col. Hugh L. Southall, USAF	**22b. TELEPHONE** *(Include Area Code)* (617) 981-2330	**22c. OFFICE SYMBOL** ESD/TML

DD FORM 1473, 84 MAR   83 APR edition may be used until exhausted.
All other editions are obsolete.

MASSACHUSETTS INSTITUTE OF TECHNOLOGY
LINCOLN LABORATORY

SOLID STATE RESEARCH

QUARTERLY TECHNICAL REPORT

1 AUGUST — 31 OCTOBER 1988

ISSUED 7 MARCH 1989

Approved for public release; distribution unlimited.

ABSTRACT

This report covers in detail the research work of the Solid State Division at Lincoln Laboratory for the period 1 August through 31 October 1988. The topics covered are Electrooptical Devices, Quantum Electronics, Materials Research, Submicrometer Technology, Microelectronics, and Analog Device Technology. Funding is provided primarily by the Air Force, with additional support provided by the Army, DARPA, Navy, SDIO, NASA, and DOE.

TABLE OF CONTENTS

LIST OF ILLUSTRATIONS

INTRODUCTION

1. SOLID STATE DEVICE RESEARCH

Microwave bandpass modulators using Mach-Zehnder interferometers in lithium niobate with periodic phase reversal electrodes have been developed for operation at 1.3 μm. Experimental results from 10- and 21-GHz modulators were found to be in good agreement with theory.

The mass transport phenomenon on etched compound semiconductors has been modeled theoretically in terms of surface-energy minimization via surface diffusion. The model yields predictions for the time evolution of any slowly varying surface profile, including a Λ^4 periodicity dependence of the decay time of sinusoidal profiles and a $t^{1/4}$ time dependence of the grading of a single mesa step.

Morphological changes of etched steps and square waves in InP have been investigated experimentally as a function of temperature and time and have been found to be in general agreement with the theoretical model of mass transport based on surface energy and surface diffusion. A relatively small activation energy of 1.5 eV has been deduced from the temperature dependence and is consistent with a surface process.

2. QUANTUM ELECTRONICS

Previous work on modeling of amplified spontaneous emission has been extended to include polarization effects and frequency dependence of the gain profile. These results show that amplified spontaneous emission can produce significant amounts of output in high-gain multistage amplifiers even when spatial apertures are used.

A 150-μm-wide, 1200-μm-long GaAs/GaAlAs single-quantum-well laser diode operating in an external cavity has produced over 1.5 W of CW output power in a spectral band of only 0.02 nm with 32-percent overall efficiency. A power of 110 mW has been obtained in a single-frequency, diffraction-limited beam.

3. MATERIALS RESEARCH

A new zone-melting-recrystallization (ZMR) configuration with enhanced radiative heating, in which the sample wafer is positioned above the movable heater, yields subboundary-free silicon-on-insulator films 0.5 μm thick over a much wider range of experimental parameters than does the conventional ZMR configuration. The principal defects in the recrystallized films are isolated threading dislocations with a density of $\sim 10^6$ cm^{-2}.

Via holes have been etched completely through the Si substrates of GaAs-on-Si wafers by using a selective plasma etching technique that permits Si to be removed at rates exceeding 20 μm/h with no apparent attack on GaAs. The exposed GaAs has a significantly better surface morphology than is generally obtained by other selective etching methods.

4. SUBMICROMETER TECHNOLOGY

The deposition of SnO_2 films has been demonstrated using an ArF (193-nm) excimer laser to drive the photochemical reactions of mixed $SnCl_4$ and N_2O vapors. Without any annealing, 100-nm-thick films grown on room-temperature substrates have resistivities as low as 0.04 ohm-cm.

Ultrashallow p^+-n junction diodes have been fabricated by laser doping using a pulsed ArF excimer laser and BCl_3 as the dopant source. Under optimized laser-doping conditions, the p^+ doping depth is about 0.1 μm and the diode characteristics show an ideality factor of unity, low reverse leakage current, and high breakdown voltage.

An ArF excimer laser has been coupled to a molecular beam epitaxy machine to allow *in situ* patterned etching of GaAs films without intervening air exposure. The mechanisms of laser-assisted chlorine etching of GaAs under high-vacuum conditions have been studied.

5. MICROELECTRONICS

A GaAs PBT has demonstrated gain in a 94-GHz experimental amplifier. Gains as high as 10 dB were achieved by taking advantage of positive internal feedback.

A 64 $\times$ 64-pixel back-illuminated CCD imager has been built for use as a wavefront sensor in an adaptive optics system. This imager has reflection-limited quantum efficiency over the visible spectrum and can operate at 2000 frames per second with a corresponding noise equivalent signal as low as 20 electrons.

Resonant tunneling devices fabricated from the InGaAs/AlAs material system have performance advantages over those made from the conventional GaAs/AlGaAs materials. Double-barrier diodes consisting of $In_{0.53}Ga_{0.47}As$ quantum wells and AlAs barriers have demonstrated peak-to-valley ratios of 28:1 at room temperature and 70:1 at 77 K, and have yielded oscillations at frequencies up to 28 GHz.

6. ANALOG DEVICE TECHNOLOGY

The loss factor of Nb-electrode thin-film capacitors has been decreased by a factor of 3 by replacing the Nb_2O_5 dielectric layer by Ta_2O_5. The Q factors of L-C resonators fabricated using this new process are greater than 1500 in the 10- to 20-MHz range.

$YBa_2Cu_3O_x$ thin films have been deposited by sequential RF diode sputtering from Y_2O_3, BaF_2, and CuO targets. The highest zero-resistance temperature of the films deposited on ZrO_2 substrates is 80 K, and the film surface is smooth and suitable for patterning by standard photolithographic techniques.

The surface resistance R_s of superconducting bismuth-strontium-calcium-copper-oxide has been measured at 4.2 K from 500 MHz to 10 GHz using a stripline-resonator technique. The value of R_s increases from $\sim 10^{-3}$ $\Omega/\square$ at 500 MHz to 10^{-1} $\Omega/\square$ at 10 GHz, close to the frequency squared dependence characteristic of the surface resistance of superconductors.

REPORTS ON SOLID STATE RESEARCH

1 August Through 31 October 1988

PUBLISHED REPORTS

Journal Articles

JA No.

6052	Optical Wavefront Measurement and/or Modification Using Integrated Optics	R.H. Rediker T.A. Lind B.E. Burke	J. Lightwave Technol. 6, 916 (1988) and IEEE J. Quantum Electron., Joint Special Issue
6056	Molecular-Beam Epitaxially Grown Spatial Light Modulators with Charge-Coupled-Device Addressing	W.D. Goodhue B.E. Burke B.F. Aull K.B. Nichols	J. Vac. Sci. Technol. A 6, 2356 (1988)
6061	Sensitivity of Quantitative Vibrational CARS Spectroscopy to Saturation and Stark Shifts	M. Péalat* M. Lefebvre* J-P.E. Taran* P.L. Kelley	Phys. Rev. A 38, 1948 (1988)
6069	Optical Nonlinearities in $Al_xGa_{1-x}As/GaAs$ Asymmetric Coupled Quantum Wells	H.Q. Le J.V. Hryniewicz W.D. Goodhue V.A. Mims	Opt. Lett. 13, 859 (1988)
6076	Fundamental Oscillations Up to 200 GHz in Resonant Tunneling Diodes and New Estimates of Their Maximum Oscillation Frequency from Stationary-State Tunneling Theory	E.R. Brown W.D. Goodhue T.C.L.G. Sollner	J. Appl. Phys. 64, 1519 (1988)
6106	Reduction of Intermodulation Distortion in Interferometric Optical Modulators	L.M. Johnson H.V. Roussell	Opt. Lett. 13, 928 (1988)

---

* Author not at Lincoln Laboratory.

* Author not at Lincoln Laboratory.

Meeting Speeches

MS No.

7503	Experimental Evaluation of Drift and Nonlinearities in Lithium Niobate Interferometric Modulators	G.E. Betts · L.M. Johnson	*Integrated Optical Circuit Engineering V*, Proc. SPIE **835**, 29 (1988), DTIC AD-A198029
7553	Advanced Device Fabrication with Angled Chlorine Ion-Beam-Assisted Etching	W.D. Goodhue S.W. Pang M.A. Hollis J.P. Donnelly	Proc. 1987 IEEE/Cornell Conf., Ithaca, New York, 10-12 August 1987, pp. 239-246
7563	Current Directions in Resonant Tunneling Research	T.C.L.G. Sollner	Proc. 1987 IEEE/Cornell Conf., Ithaca, New York, 10-12 August 1987, pp. 335-346
7570	High Power-Added Efficiency Measured at 1.3 and 20 GHz Using a GaAs Permeable Base Transistor	K.B. Nichols M.A. Hollis C.O. Bozler M.A. Quddus L.J. Kushner R. Mathews A. Vera S. Rabe R.A. Murphy D.L. Olsson	Proc. 1987 IEEE/Cornell Conf., Ithaca, New York, 10-12 August 1987, pp. 307-315
7584	A New Method to Detect Ballistic Electrons in GaAs	E.R. Brown W.D. Goodhue	Proc. 1987 IEEE/Cornell Conf., Ithaca, New York, 10-12 August 1987, pp. 326-335
7660	Fabrication of Miniature Lenses and Mirrors for InGaAsP/InP Lasers	D.Yap Z.L. Liau J.N. Walpole V. Diadiuk	*Miniature Optics and Lasers*, Proc. SPIE **898**, 18 (1988)
7926	Monolithic GaAs/Si Integration: Status and Prospects	H.K. Choi	Proc. 1988 Intl. Electronic Devices and Materials Symp., Kaohsiung, Taiwan, 29-31 August 1988, p. 21

UNPUBLISHED REPORTS

Journal Articles

JA No.

6059	Lateral Confinement of Micro-chemical Surface Reactions: Effects on Mass Diffusion and Kinetics	H.J. Zeiger D.J. Ehrlich	Accepted by J. Vac. Sci. Technol.
6068	Analysis of Conduction in Fully Depleted SOI MOSFETs	K.K. Young	Accepted by IEEE Trans. Electron Devices
6095	Short-Channel Effect in Fully Depleted SOI MOSFETs	K.K. Young	Accepted by IEEE Trans. Electron Devices
6100A	Oscillators Using Magnetostatic-Wave Active Tapped Delay Lines	C.L. Chen A. Chu L.J. Mahoney W.E. Courtney R.A. Murphy J.C. Sethares	Accepted by IEEE Trans. Microwave Theory Tech.
6104	Harmonic Multiplication Using Resonant Tunneling	T.C.L.G. Sollner E.R. Brown W.D. Goodhue C.A. Correa	Accepted by J. Appl. Phys.
6123	Growth of Beam Perturbations by Stimulated Light by Light Scattering in the Atmosphere	P.L. Kelley J-P.E. Taran*	Accepted by Appl. Opt.
6183	Defect Related Dielectric Break-down, Charge Trapping and Interface State Generation of Gate Oxides Grown on ZMR SOI Films	C-T. Lee C.K. Chen	Accepted by J. Appl. Phys.
6201	Validation of Model of External-Cavity Semiconductor Laser and Extrapolation from Five-Element to Multi-element Fiber-Coupled High-Power Laser	R.H. Rediker C.J. Corcoran L.Y. Pang S.K. Liew	Accepted by IEEE J. Quantum Electron., Special Issue

---

* Author not at Lincoln Laboratory.

Meeting Speeches*

---

* Titles of Meeting Speeches are listed for information only. No copies are available for distribution.

† Author not at Lincoln Laboratory.

---

* Author not at Lincoln Laboratory.

MS No.

7882A	Bulk-Acoustic-Wave Resonators Using Holographic Reflection Gratings in Photorefractive Materials	D.E. Oates J.Y. Pan	Seminar, ETH, Zurich, Switzerland, 1 September 1988
7882C	Bulk-Acoustic-Wave Resonators Using Holographic Reflection Gratings in Photorefractive Materials	D.E. Oates J.Y. Pan	Seminar, Schlumberger Central Research Laboratory, Paris, France, 5 September 1988
8107	SAW/FET Programmable Transversal Filter	D.E. Oates	
7892A	Techniques for Monolithically Integrating GaAs/AlGaAs Lasers of Different Wavelengths	W.D. Goodhue J.P. Donnelly J.J. Zayhowski	American Vacuum Society 9th MBE Workshop, Purdue University, West Lafayette, Indiana, 21-23 September 1988
8153	Luminescence of (AlGa)As and GaAs Grown on the Vicinal (511) B-GaAs Surface by Molecular Beam Epitaxy	E. Towe* H.Q. Le J.V. Hryniewicz C.G. Fonstad*	
7937	High-Performance IrSi Schottky-Barrier Infrared Detectors with 10-μm Cutoff Wavelength	B-Y. Tsaur M.M. Weeks* P.W. Pellegrini*	IRIS Specialty Group on Infrared Detectors, Laurel, Maryland, 16-18 August 1988
7947	Superconducting Thin Films of BiSrCaCuO Made by Sequential Electron Beam Evaporation	J.W. Steinbeck* A.C. Anderson B-Y. Tsaur A.J. Strauss	
7948	Low-Loss Lumped Element Capacitors for Superconductive Integrated Circuits	M. Bhushan J.B. Green A.C. Anderson	1988 Applied Superconductivity Conf., San Francisco, California, 21-25 August 1988
7950	Process Control for the Low Temperature Deposition of Niobium-Nitride Thin Films	A.C. Anderson D.J. Lichtenwalner W.T. Brogan	
7951	Processing of Thick-Film Dielectrics Compatible with Thin-Film Superconductors for Analog Signal Processing Devices	S.C. Wong A.C. Anderson D.A. Rudman*	

---

* Author not at Lincoln Laboratory.

MS No.

7965	Analog Nonvolatile Memory for Neural Network Implementations	J.P. Sage R.S. Withers K.E. Thompson	
7972	A Wafer Scale Thinning Process for High-Performance Silicon Devices	C.M. Huang B.B. Kosicki B.E. Burke A.C. Anderson	174th Meeting, The Electrochemical Society, Chicago, Illinois, 9-14 October 1988
8058	Microwave Circuit Applications of High-T_c Superconducting Thin Films	A.C. Anderson R.W. Ralston R.S. Withers	
8070	Mass Transport: A Promising New Technique for Compound Semiconductor Device Fabrication	Z.L. Liau J.N. Walpole	
7986	Extraction Efficiency in Q-Switched Nd^{3+} Lasers	T.Y. Fan	
8019	Amplified Spontaneous Emission in a $Ti:Al_2O_3$ Amplifier	P.A. Schulz K.F. Wall R.L. Aggarwal	Optical Society of America Annual Meeting, Santa Clara, California, 31 October – 4 November 1988
8030	Femtosecond $Ti:Al_2O_3$ Injection Seeded Laser	P.A. Schulz M.J. LaGasse* R.W. Schoenlein* J.G. Fujimoto	
8001	SAW/FET Programmable Filter with Varistor Taps for Improved Performance	D.E. Oates D.L. Smythe J.B. Green R.S. Withers	1988 IEEE Ultrasonics Symp., Chicago, Illinois, 3-4 October 1988
8017	A Comparison of Superconductive and Surface-Acoustic-Wave Signal Processing	R.S. Withers	
8069	A Review of Excimer Laser Projection Lithography	D.J. Ehrlich M. Rothschild	Microcircuits Engineering, Vienna, Austria, 20 September 1988
8086	Tunable $Ti:Al_2O_3$ Laser for Agile-Beam Optical Radar	A. Sanchez	IRIS Active Systems Conf., National Bureau of Standards, Boulder, Colorado, 18-20 October 1988

* Author not at Lincoln Laboratory.

MS No.

8099	Performance Characteristics of CCDs for the ACIS Experiment	G. Gamire* J. Nousek* D. Burrows* G. Ricker* M. Bautz* J. Doty* S. Collins* J. Janesick* R.W. Mountain B.E. Burke	SPIE Intl. Technical Symp., San Diego, California, 14-19 August 1988
8100	Fano-Noise-Limited CCDs	J. Janesick* T. Elliott* R. Bredthauer* C. Chandler* B.E. Burke	
8114	Superconductive Analog Signal Processors	R.S. Withers	U.S.-Japan Workshop, Josephson Junction Electronics, Berkeley, California, 26 August 1988
8120	Advances in Laser-Controlled Selected-Area Processing	D.J. Ehrlich M. Rothschild J.G. Black	American Vacuum Society, Atlanta, Georgia, 5 October 1988
8124	Capless Rapid Thermal Annealing of Si- and Be-Implanted InP	J.D. Woodhouse M.C. Gaidis J.P. Donnelly	Heatpulse Owners Technology Meeting, Boston, Massachusetts, 12 September 1988
8129	The Role of Implementation Technology in Neural Network Research	J.P. Sage	Intl. Neural Network Society Meeting, Boston, Massachusetts, 9 September 1988
8151	Subboundary-Free Silicon-on-Insulator Thin Films by Zone-Melting Recrystallization with Enhanced Radiative Heating	C.K. Chen J.S. Im	1988 SOS/SOI Technology Workshop, St. Simons Island, Georgia, 3-5 October 1988
8156	Excimer Laser Projection Lithography	M. Rothschild	Seminar, Raytheon Research Center, Lexington, Massachusetts, 29 September 1988

* Author not at Lincoln Laboratory.

ORGANIZATION

SOLID STATE DIVISION

A.L. McWhorter, *Head*
I. Melngailis, *Associate Head*
E. Stern, *Associate Head*
J.F. Goodwin, *Assistant*

N.L. DeMeo, Jr., *Associate Staff*

SUBMICROMETER TECHNOLOGY

D.J. Ehrlich, *Leader*
D.C. Shaver, *Assistant Leader*

Astolfi, D.K.	Lyszczarz, T.M.
Black, J.G.	Maki, P.A.
Dennis, C.L.	Melngailis, J.†
Doran, S.P.	Pang, S.W.
Efremow, N.N., Jr.	Rooks, M.J.
Forte, A.R.	Rothschild, M.
Gajar, S.A.*	Sedlacek, J.H.C.
Geis, M.W.	Uttaro, R.S.
Horn, M.W.	Young, E.M.
Kunz, R.R.	Young, K.-L.

QUANTUM ELECTRONICS

A. Mooradian, *Leader*
P.L. Kelley, *Associate Leader*
A. Sanchez-Rubio, *Assistant Leader*

Aggarwal, R.L.	Le, H.Q.
Barch, W.E.	Menyuk, N.†
Belanger, L.J.	Ochoa, J.R.
Daneu, V.	Schulz, P.A.
DeFeo, W.E.	Seppala, J.P.
Fan, T.Y.	Sharfin, W.F.
Hancock, R.C.	Sullivan, D.J.
Henion, S.R.	Tapper, R.S.
Hotaling, T.C.	Wall, K.F.
Jeys, T.H.	Zayhowski, J.J.
Lacovara, P.	

ELECTRONIC MATERIALS

A.J. Strauss, *Leader*
B-Y. Tsaur, *Associate Leader*
H.J. Zeiger, *Senior Staff*

Anderson, C.H., Jr.	Eglash, S.J.	Mastromattei, E.L.
Button, M.J.	Fahey, R.E.	Mattia, J.P.
Chen, C.K.	Finn, M.C.	Nitishin, P.M.
Choi, H.K.	Im, J.S.*	Pantano, J.V.
Clark, H.R., Jr.	Iseler, G.W.	Tracy, D.M.
Connors, M.K.	Kolesar, D.F.	Turner, G.W.
Delaney, E.J.	Krohn, L., Jr.	Wang, C.A.

* Research Assistant
† Part Time

APPLIED PHYSICS

R.C. Williamson, *Leader*
D.L. Spears, *Assistant Leader*
R.H. Rediker, *Senior Staff*

Aull, B.F.	Missaggia, L.J.
Betts, G.E.	Mull, D.E.
Bossi, D.E.*	O'Donnell, F.J.
Corcoran, C.J.*	Palmacci, S.T.
Cox, C.H., III	Palmateer, S.C.
Diadiuk, V.	Pang, L.Y.*
Donnelly, J.P.	Rauschenbach, K.
Ferrante, G.A.	Reeder, R.E.
Groves, S.H.	Roussell, H.V.
Harman, T.C.	Shiple, S.D.*
Hovey, D.L.	Tsang, D.Z.
Johnson, L.M.	Walpole, J.N.
Liau, Z.L.	Woodhouse, J.D.
Lind, T.A.	Yee, A.C.

ANALOG DEVICE TECHNOLOGY

R.W. Ralston, *Leader*
R.S. Withers, *Associate Leader*
R.M. Lerner, *Senior Staff*†

Anderson, A.C.	Lattes, A.L.
Arsenault, D.R.	Lichtenwalner, D.J.*
Bhushan, M.	Macedo, E.M., Jr.
Boisvert, R.R.	Munroe, S.C.
Brogan, W.T.	Oates, D.E.
Connelly, D.J.*	Sage, J.P.
Denneno, A.P.	Seidel, M.N.*
Fitch, G.L.	Slattery, R.L.
Green, J.B.	Thompson, K.E.
Hamm, J.M.	Yu, L-S.*
Holtham, J.H.	

MICROELECTRONICS

R.A. Murphy, *Leader*
E.D. Savoye, *Associate Leader*
B.B. Kosicki, *Assistant Leader*
R.W. Chick, *Senior Staff*

Actis, R.F.	Felton, B.J.	McIntosh, K.A.
Bales, J.W.*	Gladden, D.B.‡	Mountain, R.W.
Bennett, P.C.	Goodhue, W.D.	Nichols, K.B.
Bozler, C.O.	Gray, R.V.	Parker, C.D.
Brown, E.R.	Gregory, J.A.	Pichler, H.H.
Burke, B.E.	Hollis, M.A.	Rabe, S.
Calawa, A.R.	Huang, J.C.M.	Rathman, D.D.
Chen, C.L.	Johnson, B.W.	Reich, R.K.
Chiang, A.M.	Johnson, K.F.	Reinold, J.H., Jr.
Chuang, M.L.*	LaFranchise, J.R.	Smith, F.W.*
Clifton, B.J.	Lincoln, G.A., Jr.	Smythe, D.L., Jr.
Daniels, P.J.	Mahoney, L.J.	Sollner, T.C.L.G.
Doherty, C.L., Jr.	Manfra, M.J.	Vera, A.
Dolat, V.S.	Mathews, R.H.	Wilde, R.E.
Durant, G.L.	McGonagle, W.H.	

---

* Research Assistant
† Part Time
‡ Staff Associate

xxiv

1. ELECTROOPTICAL DEVICES

1.1 MICROWAVE BANDPASS MODULATORS IN LITHIUM NIOBATE

Microwave bandpass modulators made using Mach-Zehnder interferometers in lithium niobate with periodic phase reversal electrodes have been developed for operation at 1.3 μm. These modulators are most useful in applications requiring electrooptic modulation at a single frequency or in a range of frequencies with less than an octave bandwidth. The performance of two experimental devices, with center frequencies of 10 and 21 GHz, will be described and compared with theory. The response of the 21-GHz modulator is higher at that frequency than the response of any baseband modulator in LiNbO$_3$.

The basic principle used in these modulators is the periodic, abrupt reversal of the applied electric field along the modulator to compensate for the unequal velocities of the microwave and optical signals.[1] The phase modulation depth is calculated by integrating the voltage seen by the light as it travels along the modulator. This gives the result:

$$|\phi_m|^2 = \left(\pi \, \frac{V_m L}{R}\right)^2 2e^{-(\alpha/2)L} \left[\frac{\cosh\left(\frac{\alpha}{2} L\right) - \cos(\gamma L)}{(\gamma L)^2 + \left(\frac{\alpha}{2} L\right)^2}\right]$$

(1-1)

$$\times \left\{ \sum_{k=1}^{N} \exp[-\alpha(k-1)L] + 2 \sum_{k=1}^{N-1} \sum_{p=k+1}^{N} (-1)^{k+p} \exp\left[-\frac{\alpha}{2}(k+p-2)L\right] \cos[\gamma(p-k)L]\right\}$$

where ϕ_m is the optical phase modulation depth, R is the VL product of the modulator, L is the length of one section of the electrode, N is the number of electrode sections, V_m is the microwave voltage (peak) at the beginning of the electrode, α is the microwave power loss coefficient, and $\gamma = (\sqrt{\epsilon_{eff}} - n_{eff}) \, \omega/c$ with ϵ_{eff} the effective microwave dielectric constant, n_{eff} the effective optical mode index, and $\omega = 2\pi f$ the microwave frequency. The optical phase modulation depth refers to the phase difference between the two arms of the interferometer, and is equal to the optical intensity modulation depth for small modulation depths when the modulator is biased halfway on. The modulation depth squared is used because most applications are concerned ultimately with the RF power contained in the detected optical signal, which is proportional to the square of the optical modulation depth. The peak response occurs approximately at the frequency and section length where $\gamma L = \pi$. By putting this into Equation (1-1) and assuming $\alpha = 0$ (lossless), the peak response is seen to be proportional to N^2. This shows the motivation for using this type of modulator: the response increases enormously for large N. The trade-off is that the bandwidth decreases as N increases. The response of real devices is also limited by the microwave loss and the finite modulator length.

The experimental devices were Mach-Zehnder interferometric modulators built on Z-cut LiNbO$_3$ using Ti-indiffused waveguides. A three-section version is shown schematically in Figure 1-1. The modulator used TM-polarized light at a wavelength of 1.3 μm. The electrodes were placed over the optical waveguides, with the electrode edge lined up with the waveguide edge as shown in Figure 1-1. In this configuration, the vertical component of the electric field produced the electrooptic modulation, which allows phase reversal by simply jogging the electrodes so that the ground instead of the center electrode (or vice versa) is over the waveguide. The transition length at each phase reversal is short (55 μm), compared with the section length of 4.95 mm for the six-section device and 9.3 mm for the three-section device. The devices also had a separate electrode for dc bias (not shown in Figure 1-1).
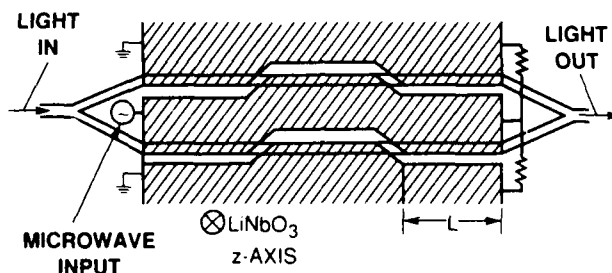
Figure 1-1. Three-section phase reversal modulator on Z-cut LiNbO$_3$.

Figure 1-2 shows the response of the three-section device. The experimental device has a peak response of 0.0116 rad^2/mW at 9.9 GHz and a 3-dB (electrical) bandwidth of $\approx$7 GHz. [The response figure of merit used in this report is the (peak) phase modulation depth squared per milliwatt of rms RF power input from a 50-Ω source.] The frequency response was measured using the swept frequency technique.[2] Figure 1-2 also shows the theoretical response calculated from Equation (1-1). The calculation used three sections of length 9.3 mm, a VL product of 76 V-mm, a microwave loss coefficient of $0.007 + 0.019\sqrt{f(GHz)}$ mm^{-1}, an ϵ_{eff} of 12.0 and an n_{eff} of 2.16; the modulator electrode impedance of 23 Ω and input impedance of 38 Ω were used to convert the input RF power to the voltage V_m on the modulator (a quarter-wave transformer was fabricated on the LiNbO$_3$ chip to match the modulator impedance to 50 Ω). These values are all consistent with direct measurements of these parameters on this or similar devices. It can be seen in Figure 1-2 that the experimental measurements match the theoretical calculation very closely.

A six-section device was also fabricated. This device had a peak response of 0.0069 rad^2/mW at 21 GHz and a 3-dB (electrical) bandwidth of $\approx$8 GHz. The theoretical calculation for this device (using the same parameters as for the t.ree-section device, except that here there are six sections of length 4.95 mm, ϵ_{eff} of 12.3, and input impedance of 20.5 Ω) approximately matches the experimental data near the peak response frequency, but the match is poor at low frequencies. We do not yet understand the reason for the increased response at low frequencies; however, the theory is still accurate in the region of interest for applications.

2
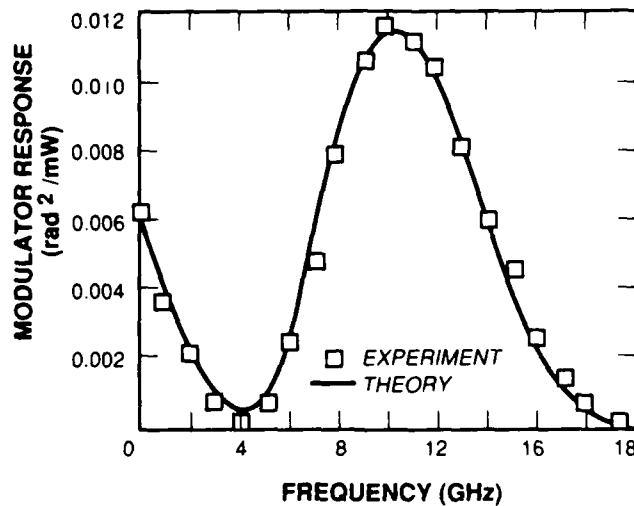
Figure 1-2.   Response of three-section modulator compared with theoretical calculation.

These modulators were also tested for large signal modulation. The RF power required for 50-percent optical intensity modulation (ϕ_m = 0.524 rad) was 22.5 mW at 10 GHz for the three-section device, and 46 mW at 20 GHz for the six-section device.

The improvement in peak response of these periodic-phase-reversal modulators as compared with baseband modulators is greater at higher frequencies; the six-section, 21-GHz device described above shows this advantage most clearly. The response of the six-section device at 21 GHz is 12 dB higher than the response of a single-section device that is identical to one section of the six-section device. For single-frequency operation at high frequencies, baseband modulators using pseudorandom coded phase reversal also appear to be less sensitive than the periodic-phase-reversal device demonstrated here. The most responsive pseudorandom device at 21 GHz so far reported[3] would require about 120 mW on the modulator electrodes for 50-percent modulation depth.

In summary, we have experimentally demonstrated bandpass modulators using electrical phase reversal. We have shown that the measured performance matches the performance calculated theoretically. The sensitivity of these devices as well as their microwave design allowed us to demonstrate large-signal modulation without excessive heating problems. Finally, we have demonstrated a modulator whose response at 21 GHz exceeds that of any baseband device in lithium niobate.

G.E. Betts
K.G. Ray

3

1.2 SURFACE-ENERGY AND TEMPERATURE EFFECT ON ETCHED STRUCTURES IN COMPOUND SEMICONDUCTORS — MODEL OF THE MASS TRANSPORT PHENOMENON

Thermally induced drastic morphological changes have recently been observed on etched InP, GaAs, and GaP mesa structures and have been used to fabricate several new optoelectronic devices.[4] An attempt has been made in this work to construct a theoretical model of the mass transport process. This model is based on surface energy and surface diffusion and is similar to one previously developed for metals.[5]

Consider an addition of a volume element dV to a curved InP surface, as illustrated in Figure 1-3. Because of the surface curvature, the addition of dV results in an increase of surface area, ds. Since extra work is needed to create a new surface, there is extra energy (i.e., the surface energy) stored in dV of an amount αds, where α is the coefficient of surface tension.[6] (Note
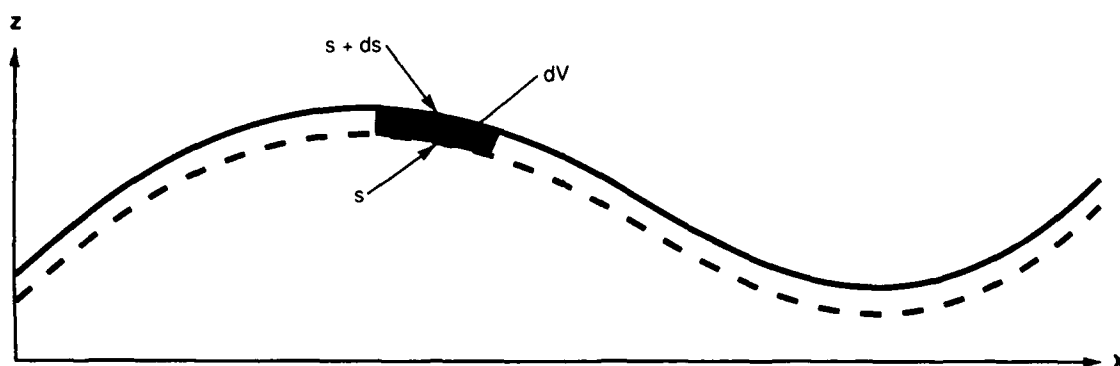
Figure 1-3.   Schematic drawing of a surface profile and the surface energy.

that a flat surface has ds = 0 and is defined as having zero surface energy.) Therefore, the surface energy per atom is

$$\epsilon = \frac{\alpha ds}{dV/v} \tag{1-2}$$

where v is the average volume of an atom. On the other hand, for a one-dimensional surface profile, we have[6]

$$\frac{ds}{dV} = \frac{1}{r} \tag{1-3}$$

where r is the radius of curvature of the surface element s. For a slowly varying profile ($\partial z/\partial x \ll 1$, where z and x are height and position, respectively), the curvature is simply

$$\frac{1}{r} \approx -\frac{\partial^2 z}{\partial x^2} \quad . \tag{1-4}$$

4

Combining Equations (1-2), (1-3), and (1-4), we have

$$\epsilon = -\alpha v \ \frac{\partial^2 z}{\partial x^2} \ . \tag{1-5}$$

The effect of surface curvature on surface dissociation and the resulting mass transport can now be considered as follows. It is well known experimentally that, at an elevated temperature, some dissociation occurs at the surface and a minimum phosphorus vapor pressure has to be supplied in the gas flow to prevent the sample from being transformed into metallic In. Such a process must result in some form of "free In atoms" which are in equilibrium with the phosphorus in the vapor and with the InP crystal. We further assume that the free In atoms exist primarily on the crystal surface with a negligibly low concentration in the vapor. (Otherwise, a significant evaporation loss would have been experimentally observed without an external supply of In vapor in the gas flow.) Let E_b be the binding energy in this dissociation process on a flat surface, and N_s the total number of In atoms per unit area. Then, the equilibrium surface concentration of free In atoms on a flat surface is given by

$$N_o = N_s e^{-E_b/k_B T} \tag{1-6}$$

where k_B and T are the Boltzmann constant and absolute temperature, respectively. For a curved surface, the surface energy ϵ represents a decrease in the binding energy and the equilibrium concentration therefore becomes

$$N = N_s e^{-(E_b - \epsilon)/k_B T}$$
$$= N_o e^{\epsilon/k_B T} \ . \tag{1-7}$$

The deviation in the surface concentration, $n \equiv N - N_o$, is then given by

$$n = N_o (e^{\epsilon/k_B T} - 1) \ . \tag{1-8}$$

It can readily be shown that, for parameter ranges of interest, $\epsilon \ll k_B T$ and $\exp[\epsilon/k_B T] - 1 \approx \epsilon/k_B T$. Hence, by using Equation (1-5), Equation (1-8) can be written as

$$n \approx - \ \frac{\alpha v N_o}{k_B T} \ \frac{\partial^2 z}{\partial x^2} \ . \tag{1-9}$$

When there is a variation of curvature across the surface, free In atoms will diffuse from regions of large curvature, where n is large, to regions of small (or negative) curvature, where these In atoms find themselves exceeding the equilibrium concentration and have to be re-incorporated into the crystal lattice. This results in the mass transport, as illustrated in Figure 1-4. Although the entire process involves a concurrent diffusion of P, the diffusion of In atoms is likely the rate-limiting process, because of the high concentration of P and the fast vapor-phase diffusion.

The conservation of mass (i.e., the continuity equation) can then be expressed as

$$D \frac{\partial^2 n}{\partial x^2} = \frac{1}{v} \ \frac{\partial z}{\partial t} + \frac{\partial n}{\partial t} \tag{1-10}$$

REGROWTH: DIFFUSION AND RE-INCORPORATION OF FREE In ATOMS
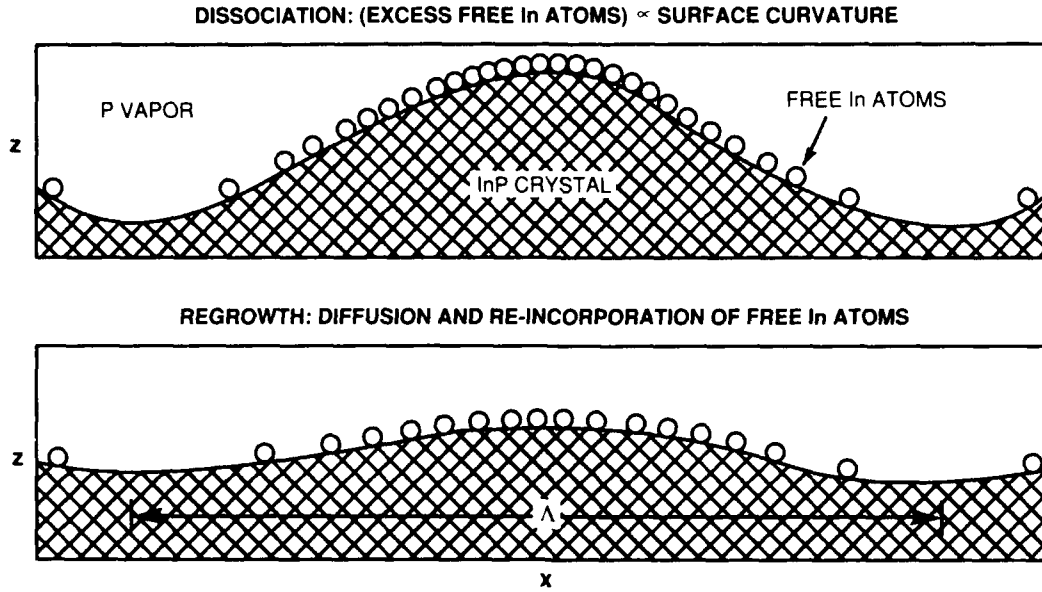
Figure 1-4.   Schematic drawing of model of mass transport.

where D is the diffusion coefficient, and t is the time. From the magnitudes of the physical parameters, it can be shown that

$$\left| \frac{\partial n}{\partial t} \right| \ll \left| \frac{1}{v} \frac{\partial z}{\partial t} \right| . \tag{1-11}$$

By further using Equation (1-9) for n, Equation (1-10) can be rearranged to become

$$-\frac{\alpha v^2 D N_o}{k_B T} \frac{\partial^4 z}{\partial x^4} = \frac{\partial z}{\partial t} . \tag{1-12}$$

For convenience, we define

$$\gamma \equiv \frac{\alpha v^2 D N_o}{k_B T} \tag{1-13}$$

and Equation (1-12) becomes

$$-\gamma \frac{\partial^4 z}{\partial x^4} = \frac{\partial z}{\partial t} . \tag{1-14}$$

Solutions of Equation (1-14) can be found by using the Fourier expansion of the initial profile $z(x,0)$. In the case of a periodic profile, a Fourier series can be used, such as

$$z(x,0) = \sum_{n=0}^{\infty} A_n \sin \left(\frac{2 n \pi x}{\Lambda} \right) \tag{1-15}$$

6

for a profile with odd symmetry about some point, where Λ is the periodicity. Then, it can easily be shown that

$$z(x,t) = \sum_{n=0}^{\infty} A_n e^{-t/\tau_n} \sin\left(\frac{2n\pi x}{\Lambda}\right) \tag{1-16}$$

satisfies Equation (1-14), provided that

$$\tau_n = \frac{1}{\gamma}\left(\frac{2n\pi}{\Lambda}\right)^{-4} . \tag{1-17}$$

Note that τ_n is proportional to $(\Lambda/n)^4$. This result suggests that a square-wave profile will quickly change into a sinusoidal one followed by an exponential decay of the latter.

Nonperiodic profiles can be treated by using Fourier integrals. For example, an initial single-step profile can be expressed as

$$z(x,0) = \frac{1}{\pi}\int_0^\infty \frac{1}{k}\sin(kx)dk \tag{1-18}$$

and the solution of Equation (1-14) becomes

$$z(x,t) = \frac{1}{\pi}\int_0^\infty \frac{e^{-\gamma t k^4}}{k}\sin(kx)dk . \tag{1-19}$$

This function can be arranged into a more useful form by defining

$$\kappa = (\gamma t)^{1/4} k \tag{1-20}$$

and

$$\xi = (\gamma t)^{-1/4} x . \tag{1-21}$$

Equation (1-19) then becomes

$$z(x,t) = \frac{1}{\pi}\int_0^\infty \frac{e^{-\kappa^4}}{\kappa}\sin(\kappa\xi)d\kappa . \tag{1-22}$$

Note that the right-hand side of Equation (1-22) defines a function $z(\xi)$, from which the surface profile at various times t is obtained simply by a coordinate expansion (scaling), $x \propto t^{1/4}$, as specified by $\xi = (\gamma t)^{-1/4} x$ in Equation (1-21). The function $z(\xi)$ has been evaluated numerically by approximating the integral with a series [which converges quickly because of the factor $\exp(-\kappa^4)$] and the result is shown in Figure 1-5. Note that $|z(\xi)|$ rises linearly from the origin and shows a 10-percent overshoot before settling to the constant value of 0.5. The overshoots have indeed been observed experimentally (see Section 1.3 below).

7
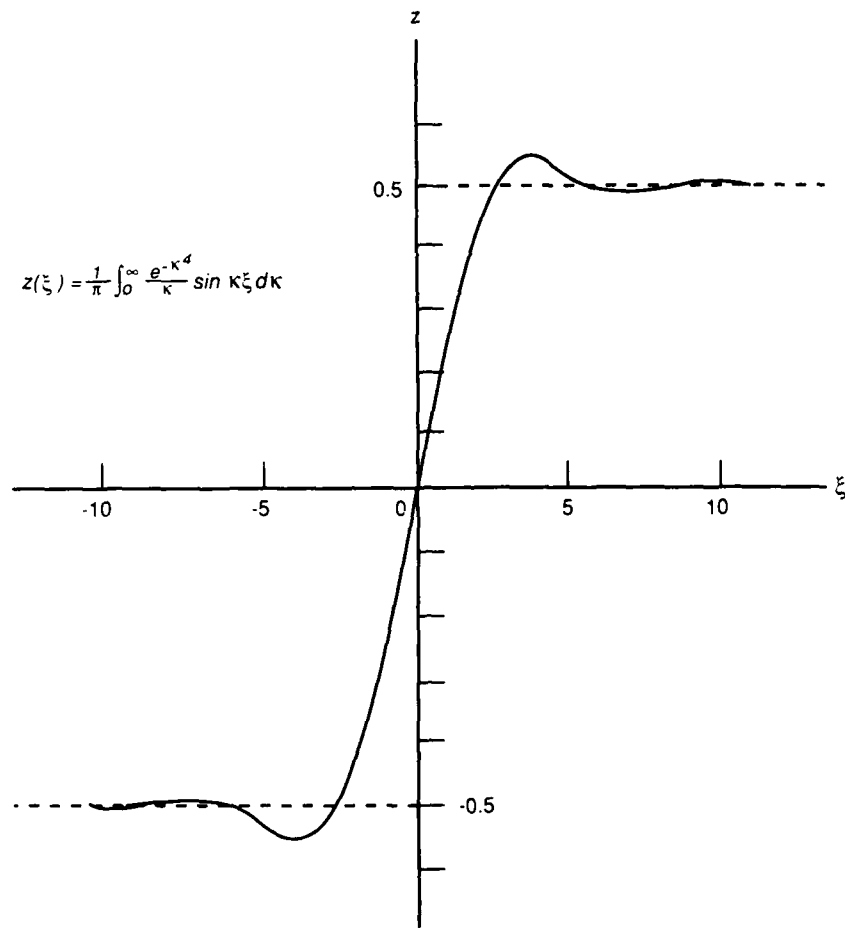
$$z(\xi) = \frac{1}{\pi} \int_0^\infty \frac{e^{-\kappa^4}}{\kappa} \sin \kappa\xi \, d\kappa$$

Figure 1-5. Function z(ξ), which can be used to describe the evolution of a single mesa step during mass transport.

The slope of $z(\xi)$ at the origin can be evaluated by taking the derivative of Equation (1-22), i.e.,

$$\frac{dz}{d\xi}\bigg|_{\xi=0} = \frac{1}{\pi} \int_0^\infty e^{-\kappa^4} d\kappa$$

$$= \frac{\Gamma\left(\frac{1}{4}\right)}{4\pi} . \tag{1-23}$$

The slope of $z(x,t)$ at the origin can then be found by using Equation (1-21), and a characteristic "transport length" can be defined as

$$L \equiv \frac{1}{(\partial z/\partial x)_{x=0}}$$

$$= \frac{4\pi}{\Gamma\left(\frac{1}{4}\right)} (\gamma t)^{1/4} \ . \tag{1-24}$$

Note that L provides a convenient measure of the extent of mass transport and has a $t^{1/4}$ time dependence.

In conclusion, a simple model has been constructed for the mass-transport phenomenon due to surface-energy minimization on etched compound semiconductors. With the use of Fourier analysis, the model yields simple solutions for any slowly varying surface profiles. In particular, it predicts a Λ^4 periodicity dependence of the decay time for sinusoidal profiles and a $t^{1/4}$ time dependence for the broadening of a single mesa step.

Z.L. Liau
H.J. Zeiger

1.3 KINETICS OF MASS TRANSPORT OF ETCHED STRUCTURES IN InP DUE TO SURFACE-ENERGY MINIMIZATION

We report an experimental investigation on the morphological changes of etched structures in InP as a function of temperature and time. The results are compared with a theoretical model based on surface energy and surface diffusion (see Section 1.2 above).

Nominally (100)-oriented, undoped InP substrates were used. The substrates were first free-etched in Br-methanol to remove polishing damages. Photolithography and chemical etching were then carried out to form mesa stripes parallel to the (01$\bar{1}$) planes. To minimize material variations, many small samples, approximately 1×4 mm each, were cleaved from one large piece for various mass-transport experiments. The samples were thoroughly cleaned and loaded into a graphite container in a furnace system.[7] After N_2 and H_2 purging, a PH_3 flow was introduced into the system. The PH_3 was diluted by purified H_2 to a concentration less than 5 percent.

In addition to the relatively small mesa height (1 to 2 μm), long mass-transport times (3 to 100 h) were used to form slowly varying surface profiles in order to comply with the approximation assumed in the theoretical model and to optimize the accuracy in the stylus surface profiling used to characterize the transported samples. Usually, a group of 3 to 4 samples were initially loaded together, but only one sample was taken out after each mass-transport period, with the rest immediately reloaded for longer times. Surface profiles of the mass-transported samples were measured by a cone-shaped stylus with a spherical tip of approximately 0.5-μm radius.

Figure 1-6 shows a square-wave mesa structure before and after mass transport at 780°C for 3.25 and 19.25 h. It can be seen that the profile first developed into a sinusoidal one, followed by a gradual decay in amplitude, as predicted by the model.
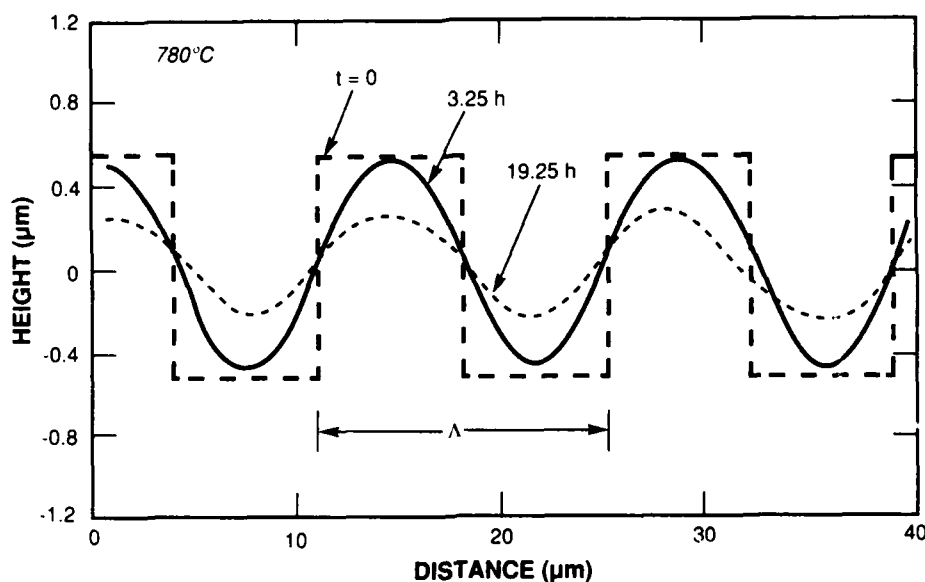
Figure 1-6. Mass transport of an etched square-wave surface profile.

Figure 1-7 shows the amplitude decay of sinusoidal profiles of various periodicities. Note that the decay initially followed an exponential law, as predicted by the model. However, it later slowed down, indicative of some deficiency of the simple model. The slowdown could also be caused by increased contamination due both to the prolonged mass transport (which also results in a phosphorus accumulation in the system) and the sample reloading procedure. To avoid these complications, the decay time τ was determined by using the first two data points. This decay time is then plotted against the periodicity Λ, as shown in Figure 1-8. Note that the results closely follow a $\tau \propto \Lambda^4$ relationship, in good agreement with the model.

Figure 1-9 shows the profiles of a wide mesa before and after mass transport. Since mass transport occurs near the mesa edge in a region considerably smaller than the mesa width, the situation is virtually that of a step function which has previously been considered theoretically in the model. Note that in Figure 1-9 the sample after mass transport has developed humps and dips close to those predicted in the model. As defined in Equation (1-24) above, the transport length L provides a quantitative measure of the mass transport and can be evaluated in the present experiment. As shown in Figure 1-10, the measured transport length approximately follows a $t^{1/4}$ dependence as predicted theoretically.

As evident in Equations (1-17) and (1-24) in Section 1.2 above, the mass-transport coefficient γ can be determined either from the decay time τ or from the transport length L. For the mass-transport temperature of 780°C for which both sets of data are available, the γ's determined were indeed nearly identical. To investigate the temperature dependence of γ, the value of L(t) has been measured for two other temperatures as shown in Figure 1-10. The resulting Arrhenius plot for γ is shown in Figure 1-11, in which an activation energy of 1.5 eV has been deduced.

10
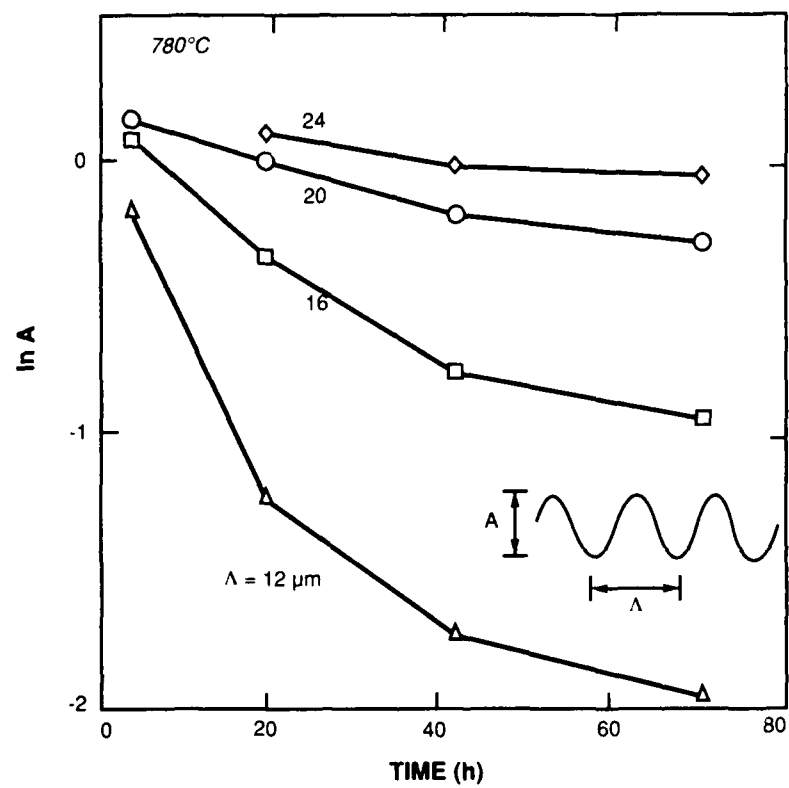
Figure 1-7. Amplitude decay of sinusoidal profiles due to mass transport.
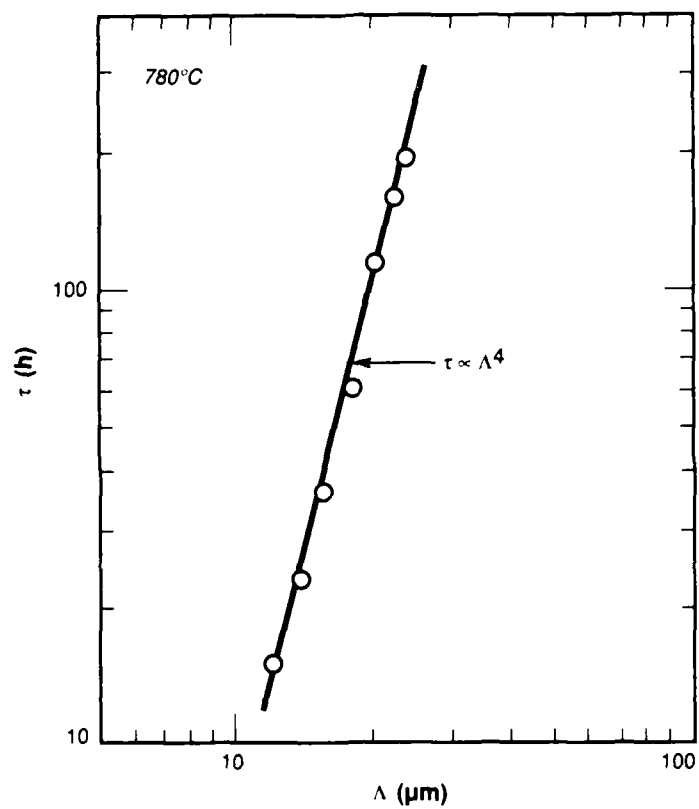
Figure 1-8. Dependence of decay time τ on the periodicity of the sinusoidal profile.
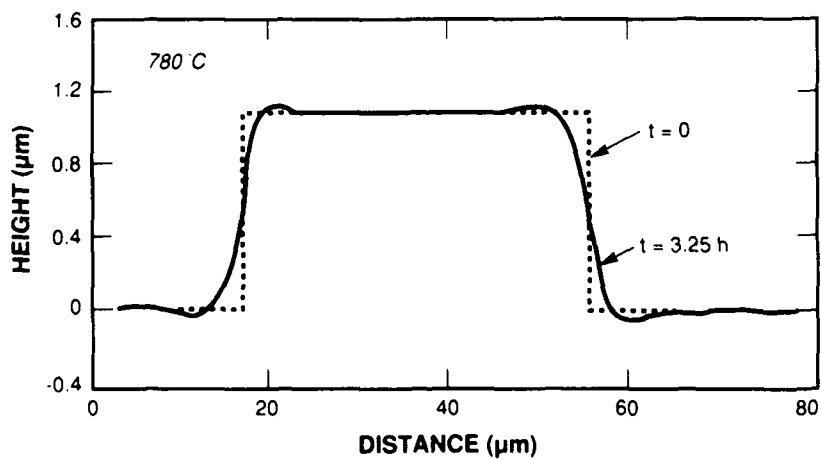
Figure 1-9. Mass transport near the edges of a wide mesa.

12
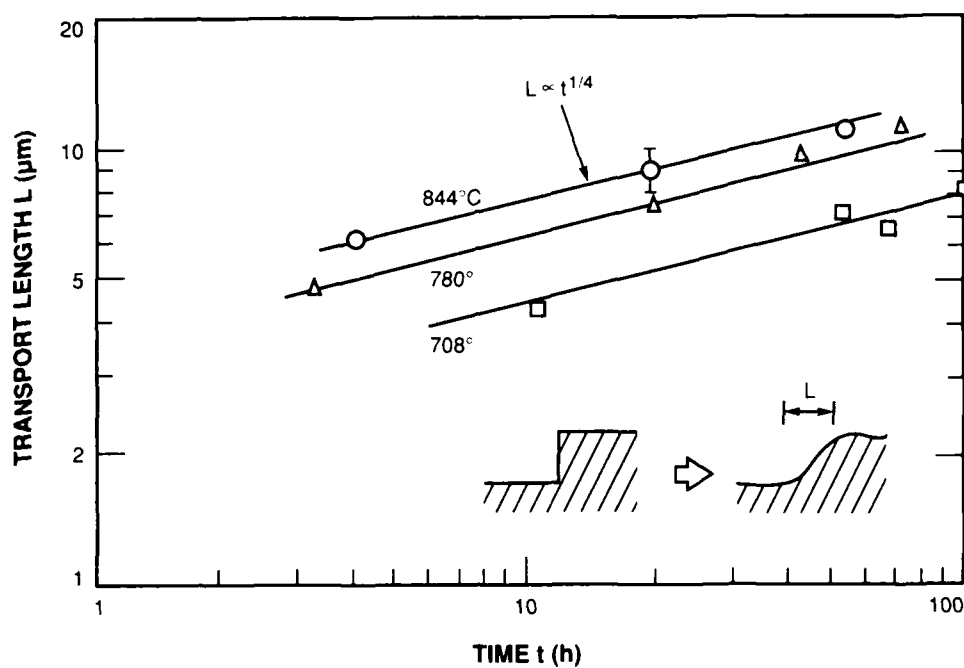
Figure 1-10. Transport length vs time of single mesa steps at three different temperatures.
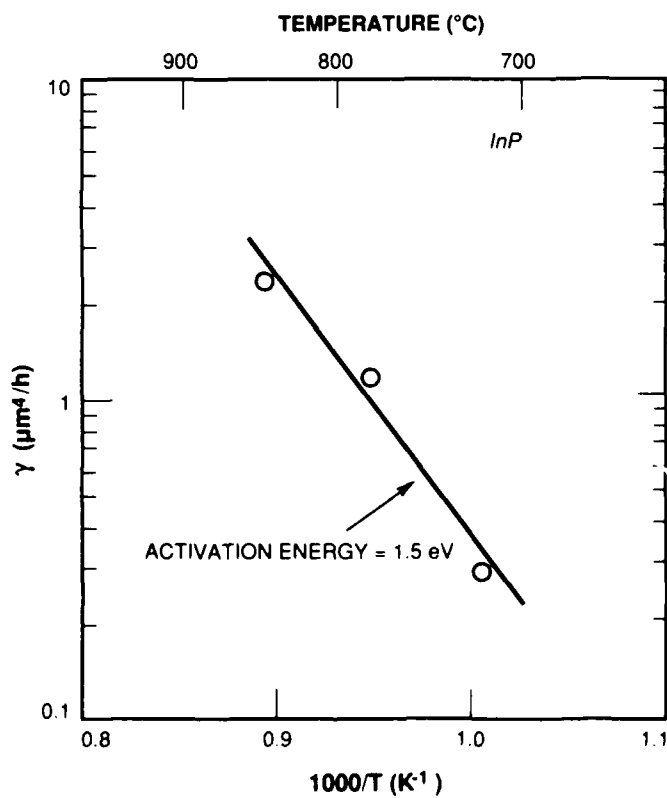
Figure 1-11. Temperature dependence of the mass-transport coefficient γ.

13

Although this activation energy is presumably the sum of two activation energies arising from the diffusion constant D and the equilibrium surface concentration N_o of free In atoms on a flat surface [see Equation (1-13) in Section 1.2], it is still rather small as expected for a surface process.

Aside from some experimental uncertainties, the present results show a general agreement with the theoretical model. The model not only provides a better understanding of mass transport, but also facilitates an improved control in the use of the phenomenon for device fabrication. In particular, the Λ^4 dependence of the sinusoidal decay time implies easy control of the lens and mirror fabrications, for the process will virtually stop after the short-period steps have been smoothed to achieve the desired lens or mirror profiles. This is consistent with experimental observations in the recent lens fabrication in which accurately controlled lens profiles have been achieved.[4,8] Furthermore, the low activation energy obtained in the present work is consistent with a surface process and is potentially advantageous in device fabrication. Mass transport can be carried out at low temperatures to avoid undesired bulk diffusion, a process that generally has a higher activation energy because of a tighter atomic binding. In fact, this could be an important reason why mass transport has already proved useful in laser fabrication.

Z.L. Liau
D.E. Mull

REFERENCES

1. R.C. Alferness, S.K. Korotky, and E.A.J. Marcatili, IEEE J. Quantum Electron. **QE-20**, 301 (1984).

2. S. Uehara, Appl. Opt. **17**, 68 (1978).

3. R.L. Jungerman, C.A. Johnsen, D.W. Dolfi, and M. Nazarathy, Electron. Lett. **23**, 172 (1987).

4. See, for example, Z.L. Liau, V. Diadiuk, J.N. Walpole, and D.E. Mull, Appl. Phys. Lett. **52**, 1859 (1988), DTIC AD-A197477.

5. See, for example, J.M. Blakely, *Introduction to the Properties of Crystal Surfaces* (Pergamon Press, Oxford, 1973), Chap. 7.

6. L.D. Landau and E.M. Lifshitz, *Statistical Physics* (Addison-Wesley, Reading, Massachusetts, 1958), Chap. 15.

7. Solid State Research Report, Lincoln Laboratory, MIT (1987:3), pp. 11-14, DTIC AD-A192837.

8. *Ibid.* (1988:3), pp. 3-6.

2. QUANTUM ELECTRONICS

2.1 A SIMPLE MODEL FOR AMPLIFIED SPONTANEOUS EMISSION SPECTRAL NARROWING

In calculating amplified spontaneous emission (ASE), the line shape of the gain must be taken into account. This problem has been treated in the literature[1], but analytic results have never been obtained. Here, we provide an analytic treatment in a form that can easily be incorporated in ASE computer programs[2] that have so far not considered the effects of the line shape. We show that ASE may cause a significant output power in high-gain multistage amplifiers, even when apertures are used between stages to minimize the solid angle under which early stages see later stages.

We assume that the line shape is Lorentzian[3]:

$$\sigma(\nu) = \frac{\sigma_0}{1 + \left(\dfrac{\nu - \nu_0}{\alpha}\right)^2} \tag{2-1}$$

where α is the half-width at half-maximum, and ν_0 is the center of the gain profile. This approximate line shape can be used for $Ti:Al_2O_3$, as well as numerous other materials. The growth of the ASE intensity through an amplifier stage, assuming the lower laser level remains unpopulated, is given by[4]

$$\frac{dI(\nu)}{dx} = \sigma(\nu)I(\nu)N + \Omega h\nu Nf(\nu) \tag{2-2}$$

where I is the ASE spectral intensity in power per unit area and unit frequency interval, N is the upper laser level density, $f(\nu)$ is the spontaneously emitted photon flux per unit solid angle and unit frequency interval for one polarization, and Ω is the solid angle under which an elemental volume producing spontaneous emission sees the exit face of the amplifier. The value of Ω depends, in principle, on the coordinate x along the length of the amplifier; but if the gain is significant, only the spontaneous emission from the early part of the amplifier plays a role. Thus, for all practical purposes Ω can be treated as a constant.[2]

The first term on the right-hand side of Equation (2-2) is the well-known stimulated emission term; it accounts for the amplification of the ASE by a thin element dx of the amplifier. The second term describes the change in ASE intensity caused by spontaneous emission in the same element dx. This second term is related[5] to the stimulated emission cross section:

$$f(\nu) = \sigma(\nu)\left(\frac{n\nu}{c}\right)^2 \tag{2-3}$$

where n is the index of refraction. If saturation is neglected, the differential equation can be cast in the form

$$\frac{dI(\nu)}{\sigma(\nu)[I(\nu) + \Omega h n^2 \nu^3/c^2]} = Ndx \quad . \tag{2-4}$$

We integrate both sides of this equation over the length L of the amplifier. The result is

$$\gamma_0 = \frac{\sigma_0}{\sigma(\nu)} \ln \left[\frac{I_{out}(\nu) + \Omega hn^2 \nu^3/c^2}{\Omega hn^2 \nu^3/c^2} \right] \tag{2-5}$$

where

$$\gamma_0 = \sigma_0 \int_0^L N dx \tag{2-6}$$

is the logarithmic small signal gain of the amplifier at the peak of the gain profile. To find the total ASE intensity emerging from the amplifier, we solve Equation (2-5) for the output intensity per unit frequency band, and then integrate over frequency:

$$I_{out} = \frac{\Omega hn^2}{c^2} \int_0^\infty \left\{ \exp\left[\gamma_0 \frac{\sigma(\nu)}{\sigma_0} \right] - 1 \right\} \nu^3 d\nu \quad . \tag{2-7}$$

The exponential function peaks quite sharply at the center of the gain profile unless γ_0 is so small that ASE is of no concern. Over the range of integration where the exponential term is large, the cube of the frequency occurring in the integrand may be treated as a constant and can be removed from the integral. The result is

$$I_{out} = \frac{\Omega hn^2 \nu_0^3 \alpha}{c^2} \int_{-\infty}^\infty \left[\exp\left(\frac{\gamma_0}{1 + u^2} \right) - 1 \right] du \tag{2-8}$$

where we have written u for $(\nu - \nu_0)/\alpha$. The integral in this expression depends on the logarithmic small signal gain of the amplifier only, so the result we have obtained holds for any amplifier material that has a Lorentzian gain profile. The integral can be expressed in terms of modified Bessel functions, I_0 and I_1, as follows:

$$F(\gamma_0) = \frac{1}{\pi} \int_{-\infty}^\infty \left[\exp\left(\frac{\gamma_0}{1 + u^2} \right) - 1 \right] du = \gamma_0 e^{\gamma_0/2} \left[I_0\left(\frac{\gamma_0}{2} \right) - I_1\left(\frac{\gamma_0}{2} \right) \right] \tag{2-9}$$

For $\gamma_0 > 2$, the asymptotic approximation

$$F(\gamma_0) \approx \frac{e^{\gamma_0}}{\sqrt{\pi \gamma_0}} \left(1 + \frac{3}{4\gamma_0} \right) \tag{2-10}$$

is correct to within 10 percent. Figure 2-1 shows a graph of the integral and this approximation.

As an example, we calculate the intensity of the ASE for a Ti:Al$_2$O$_3$ amplifier with an overall logarithmic gain of 20, i.e., a gain of 5×10^8 or 87 dB. If a fixed beam area of 0.025 cm^2 and a path length of 5.6 m are assumed, the output ASE intensity is 170 kW/cm^2. This ASE intensity would cause a factor-of-2 drop in amplifier gain in about 130 ns. It appears that the ASE allows amplifier chains for short pulses only, unless the ASE can be suppressed by, for example, the
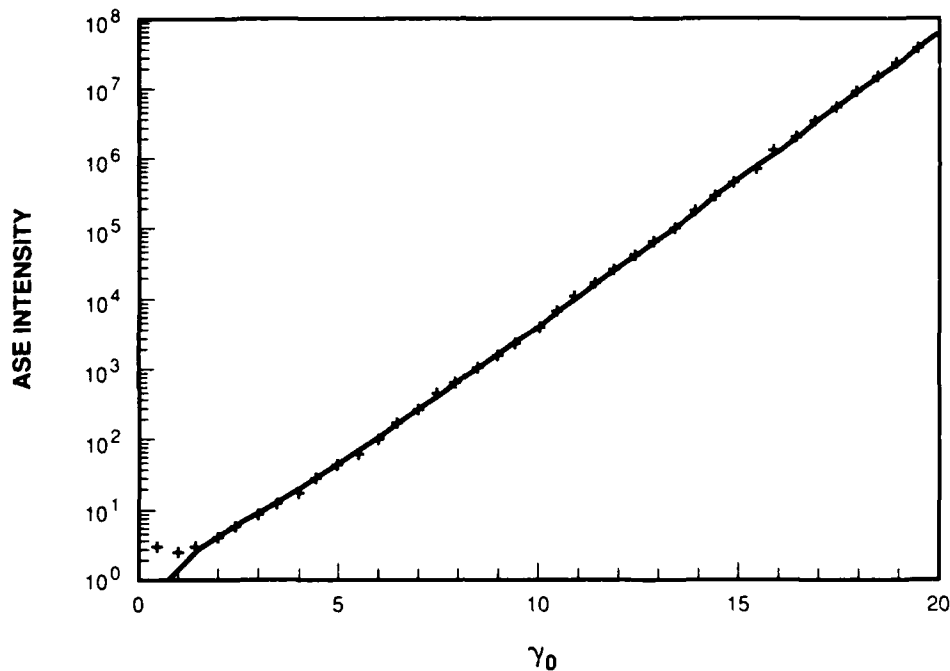
Figure 2-1. Logarithmic plot of the integral in Equation (2-9), filled circles, and the approximation given in Equation (2-10), solid line. The ASE intensity grows nearly exponentially with increasing gain.

inclusion of a spectral filter in the amplifier chain. For a top-hat gain profile, the ASE output intensity would be

$$I_{out} = \frac{2\Omega h n^2 \nu_0^3 \alpha'}{c^2} (e^{\gamma_0} - 1) \tag{2-11}$$

where α' is the half-width. If the areas under the gain profiles are equated for the two cases, then $\alpha' = \pi\alpha/2$. The only significant difference between this result and the Lorentzian case is that the factor $\sqrt{\pi\gamma_0}$ in the denominator is missing, i.e., there is no spectral narrowing.

Note that for Ti:Al$_2$O$_3$ it is appropriate to use only one polarization in the ASE calculation. The gain cross section for one polarization is significantly larger than for the other, so that the total gain for light with the less-favored polarization is insignificant. For other materials, the results of this calculation may have to be applied to each polarization separately.

In conclusion, we have derived an approximate analytic expression for the ASE to be expected in high-gain amplifiers, taking into account the spectral dependence of the gain. The Lorentzian line shape causes an effective spectral narrowing of the ASE, which reduces its intensity by a factor of about $\sqrt{\pi\gamma_0}$, typically not larger than 10.

P.A. Schulz
A. Walther

17

2.2 HIGH-POWER, DIFFRACTION-LIMITED, NARROWBAND EXTERNAL CAVITY DIODE LASER

External cavity operation has been shown to reduce nearly all of the multimode output power from a monolithic device into a single frequency.[6] Single quantum well (SQW), graded-index (GRIN), separate confinement heterostructure (SCH) diode lasers are extremely efficient devices. We have combined these properties by designing an external cavity for a GaAs/GaAlAs GRIN-SCH-SQW diode laser. This laser system has demonstrated 32-percent overall power conversion efficiency and spectral width of 0.02 nm at 1.6 W of CW output power. It has produced 110 mW of stable, single-frequency power in a diffraction-limited beam using a 0.83-A injection current. Intermittent single-frequency operation was observed at powers up to hundreds of milliwatts.

The small loss in the thin quantum well active region of our devices allows a long diode to be made without the intolerable decrease in the external quantum efficiency of a shorter device. The relatively low transparency current density and high differential gain of quantum-well devices also insures that the threshold current does not increase rapidly with length. Long devices with wide active regions can be operated at high current for high output power because their lower electrical resistance makes them less susceptible to overheating. Therefore, we used a 1.2-mm-long, 150-μm-wide device with a 5-nm-thick SQW. When coupled with an external cavity to provide spatial mode control, this diode becomes a narrow-linewidth source with high brightness.

The external cavity configuration of our laser is schematically depicted in Figure 2-2. In the narrow dimension, perpendicular to the p-n junction of the diode [Figure 2-2(a)], the optical
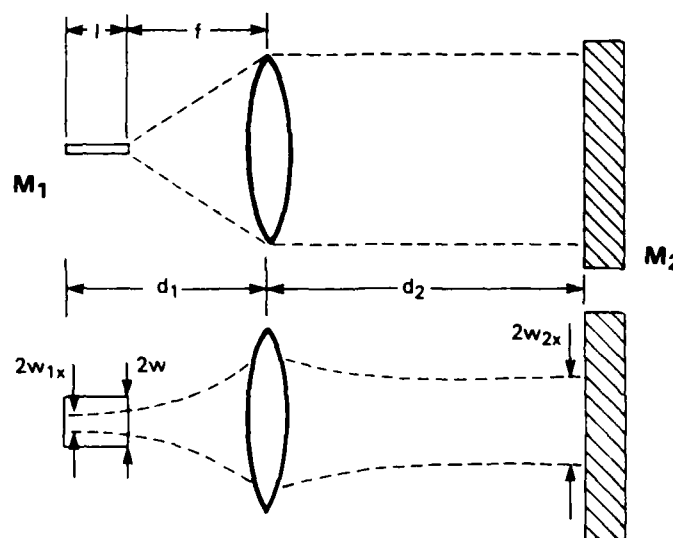
Figure 2-2.   Schematic diagram of the external cavity laser. (a) Cross section perpendicular to p-n junction of diode. The active region has length l. (b) Cross section parallel to junction plane. The active region has width 2w.

18

mode is largely guided by the graded index structure of the monolithic device. A spherical lens with a sufficiently large numerical aperture was chosen to capture all the light emitted from the diode. The mode geometry parallel to the p-n junction [Figure 2-2(b)] was controlled by proper placement of mirror M_2. If d_2 is chosen so that the diameter of the fundamental cavity mode $(2w_{1x})$ at the mirror M_1 is larger than the width of the active region $(2w)$, the laser will operate in a fundamental mode at power levels (at least hundreds of milliwatts) at which holeburning is negligible. Geometrical constraints prevented operation of the present laser in the ideal configuration, so that an aperture was required to maintain stable, single-mode operation at high power. Figure 2-3 shows the total laser power plotted against injection current. Figure 2-4(a) indicates the spectral output of the laser at over 1.5 W of total power. The trace shown was obtained from a scanned linear photodiode array in the plane of the exit slit of a 3/4-m grating spectrometer. The output of a single array element (sharp central spike) predominated with a resolution of 0.02 nm (8 GHz at the laser wavelength of 860 nm). Figure 2-4(b) shows the trace from a scanning Fabry-Perot spectrum analyzer with the laser operating at a single frequency at 110 mW. Finally, in Figure 2-5 we show the near-field (a) and far-field (b) scans of the beam cross section in the plane parallel to the p-n junction with the laser operating at single frequency. The beam was truly diffraction limited to within experimental error.

W.F. Sharfin
J.P. Seppala
A. Mooradian

REFERENCES

1. A. Yariv, *Quantum Electronics*, 2nd edition (Wiley, New York, 1975), Chap.12; L.W. Casperson and A. Yariv, IEEE J. Quantum Electron. **QE-8**, 80 (1972).

2. P.A. Schulz, K.F. Wall, and R.L. Aggarwal, Opt. Lett. **13**, 1081 (1988).

3. P.F. Moulton, J. Opt. Soc. Am. B **3**, 125 (1986).

4. L. Allen and G.I. Peters, Phys. Rev. A **8**, 2031 (1973).

5. D.E. McCumber, Phys. Rev. **134**, A299 (1964).

6. M.W. Fleming and A. Mooradian, IEEE J. Quantum Electron. **QE-17**, 44 (1981), DTIC AD-A108887.
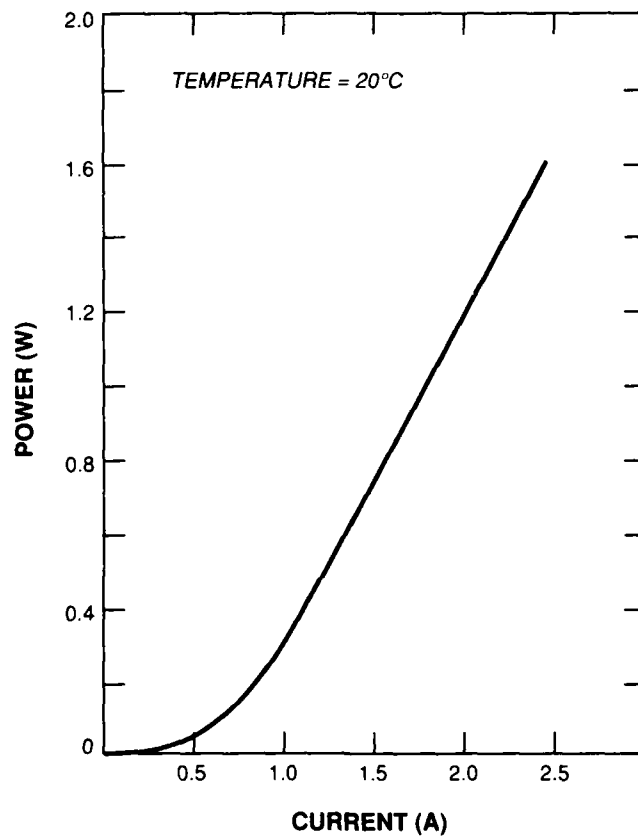
Figure 2-3. Plot of output power vs injection current for the external cavity laser.

112816-13

20
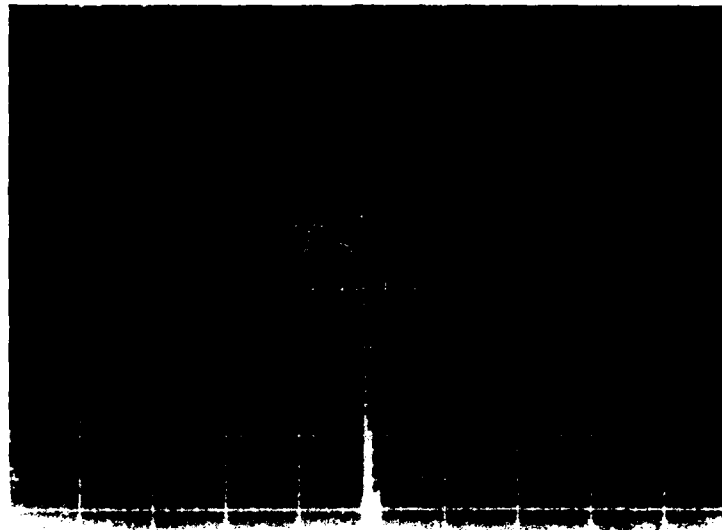
(a)
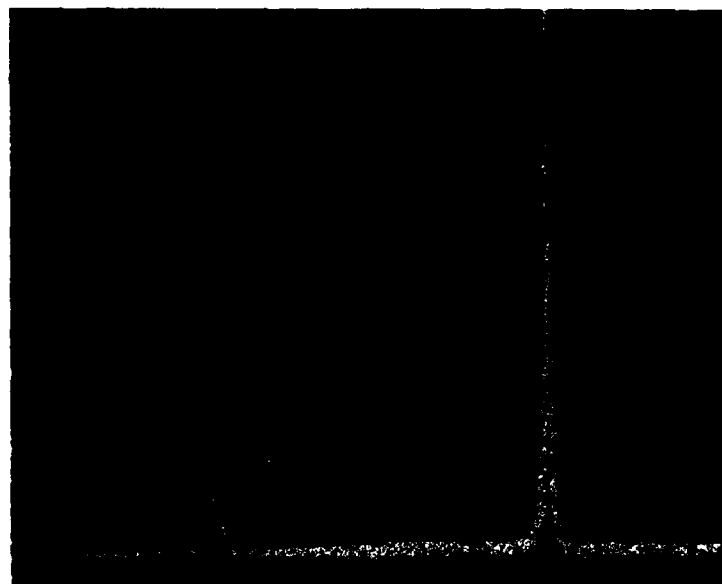
(b)

Figure 2-4. (a) Output spectrum of external cavity laser at full power. Horizontal scale is 0.6 nm/div. Arrow indicates sharp spike with 0.02 nm width. (b) Transmission of scanned Fabry-Perot interferometer showing single-frequency spectrum of laser at 110 mW.
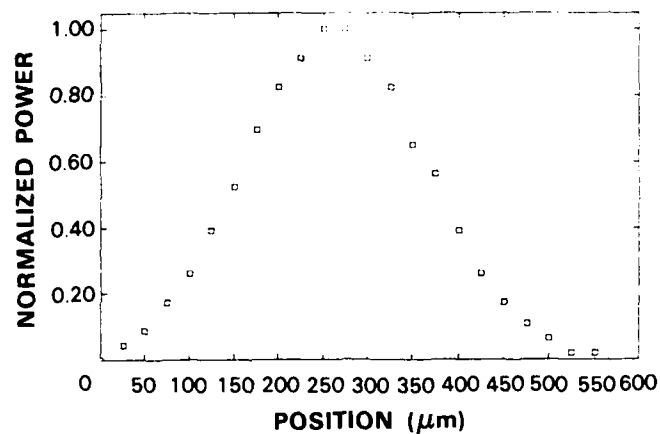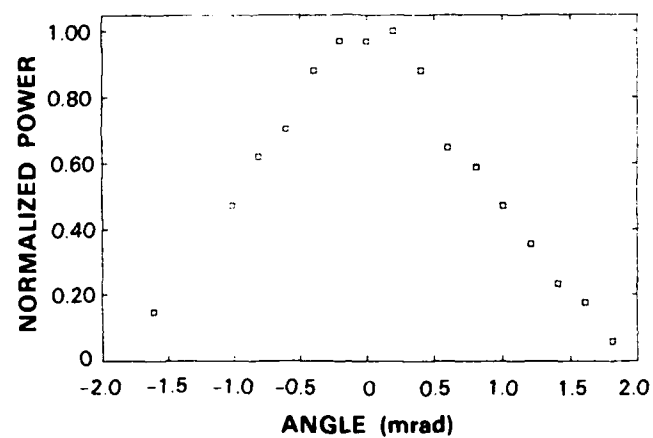
Figure 2-5. (a) Near-field beam profile of laser showing an e^{-2} intensity width of 400 μm. (b) Far-field beam profile showing all the laser power with diffraction-limited divergence.

3. MATERIALS RESEARCH

3.1 Si-ON-INSULATOR FILMS PREPARED BY ZONE-MELTING RECRYSTALLIZATION WITH ENHANCED RADIATIVE HEATING

In recent years, substantial efforts have been directed toward the development of zone-melting recrystallization (ZMR) as a means for producing high-quality silicon-on-insulator (SOI) films.[1,2] These efforts have been motivated by the potential of thin-film devices for achieving higher packing density, speed, and radiation resistance than bulk devices. When the ZMR process was first introduced, low-angle grain boundaries (subboundaries) were found to be the principal defects in the recrystallized SOI films.[3] Subsequently, a number of groups have identified conditions under which subboundary-free 1-μm-thick films can be prepared.[4-6] However, it has been very difficult to eliminate subboundaries from films with a thickness of 0.5 μm or less, which are of greater importance for large- and very-large-scale integrated-circuit applications. In this report we describe a novel ZMR configuration,[7] with enhanced radiative heating, that has enabled us to prepare subboundary-free 0.5-μm-thick SOI films over a much wider range of experimental parameters than previously possible.

Schematic diagrams of a typical SOI sample and the conventional ZMR configuration are shown in Figure 3-1. The sample is prepared by oxidizing a Si wafer, depositing successive layers
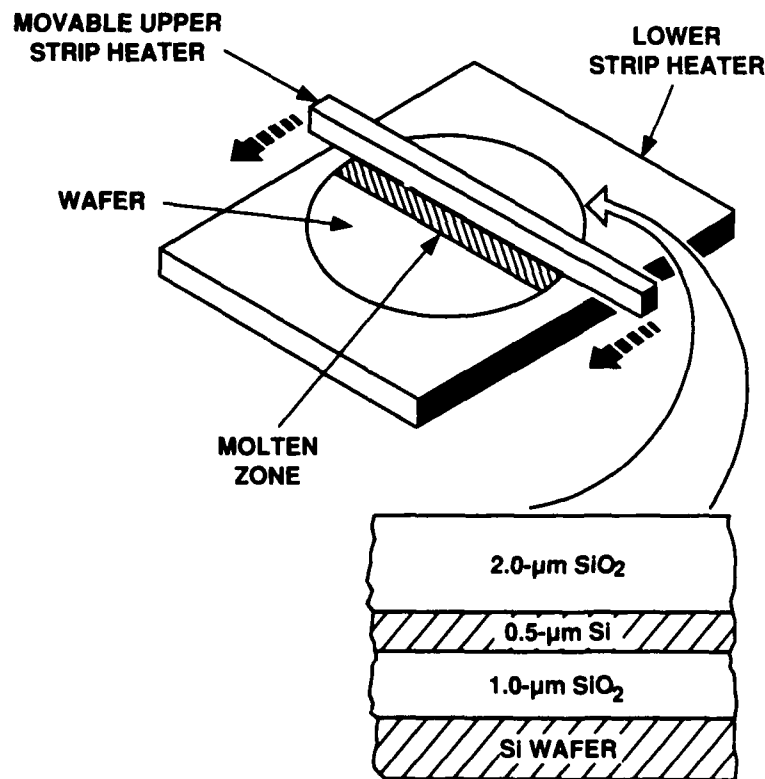
Figure 3-1. Schematic diagrams showing the conventional configuration for ZMR and the structure of a typical SOI sample.

23

of polycrystalline Si and SiO_2 by chemical vapor deposition, and annealing the wafer in ammonia to ensure wetting of the molten Si during ZMR (Reference 8). The sample is placed on the stationary lower heater and heated to a base temperature of $\sim 1100°C$ in an Ar atmosphere. Additional radiant energy from the movable upper heater is supplied to create a narrow molten zone, which is scanned across the sample to recrystallize the SOI film.

Schematic cross-sectional diagrams comparing the conventional ZMR configuration and the new configuration with enhanced radiative heating are shown in Figure 3-2. In the conventional configuration [Figure 3-2(a)], the sample is mounted between the upper and lower heaters, with the SOI film facing upward. In the new configuration, the sample is positioned above the upper heater with the film facing downward [Figure 3-2(b)].
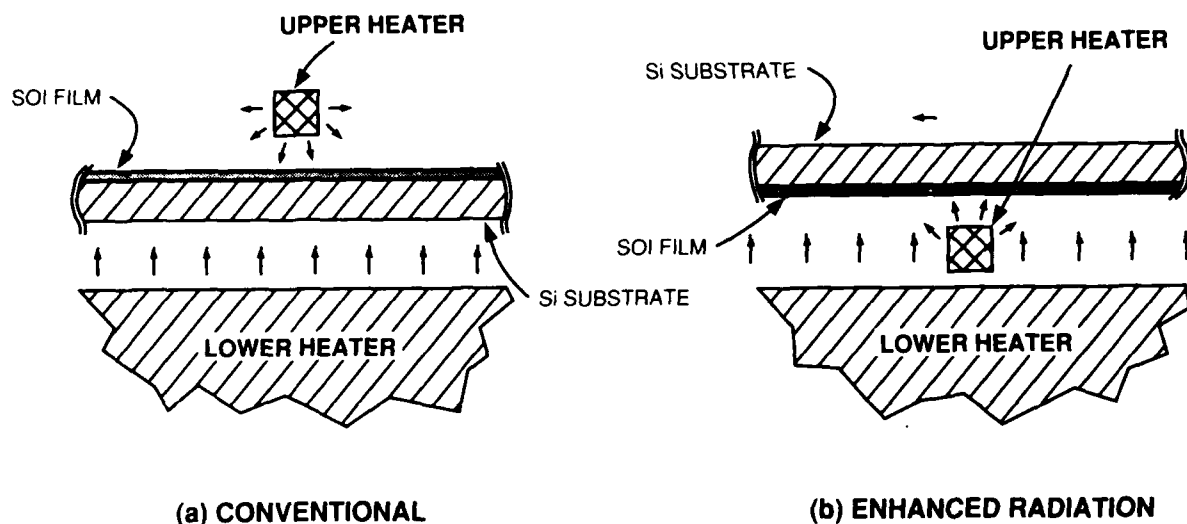
Figure 3-2. Cross-sectional diagrams showing (a) the conventional ZMR configuration and (b) the new configuration with enhanced radiative heating.

Figure 3-3 shows low- and high-magnification optical micrographs of a defect-etched subboundary-free 0.5-μm-thick SOI film prepared by ZMR using the enhanced radiative heating configuration with a tungsten upper heater 2.5 mm wide and 0.15 mm thick. As shown by both optical Nomarski and transmission electron microscopy, the principal defects are isolated threading dislocations with a density of $\sim 10^6$ cm^{-2}, the same level obtained in subboundary-free 1-μm-thick films. At a scan speed of ~ 0.1 mm/s, such subboundary-free 0.5-μm-thick films were obtained over a 5-percent range in movable heater power. In contrast, when the conventional configuration was used with the same scan speed, subboundary-free 1.0-μm-thick films could be obtained only within a range of ~ 2 percent in movable heater power, and subboundary-free 0.5-μm-thick films were not obtained at all.

24
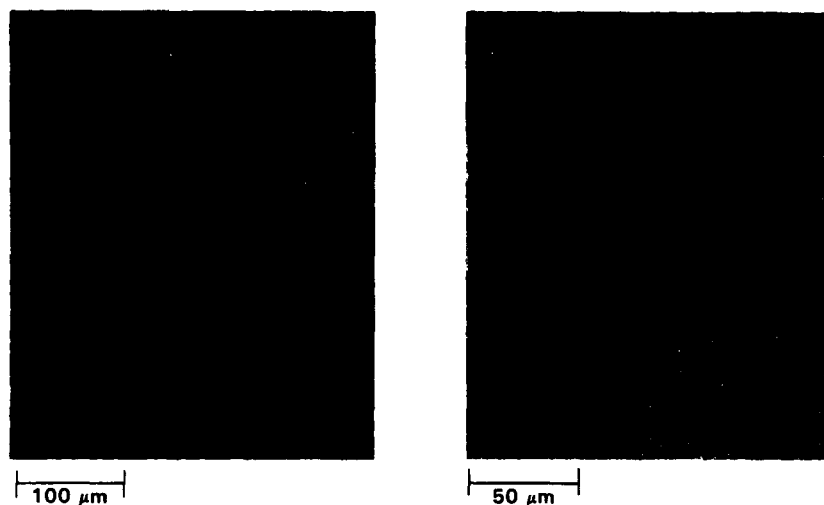
Figure 3-3.   Low- and high-magnification optical micrographs of subboundary-free defect-etched 0.5-μm-thick SOI film prepared by ZMR using enhanced radiative heating.

In previous studies using a long-working-distance zoom lens for *in situ* observation of the solid-liquid interface morphology, we found that subboundary-free films are obtained when the interface has a stable cellular interface with trailing cusps, provided that the heater power and scan speed are sufficiently low.[9] The stable cellular morphology persists even when the scanning motion is stopped, showing that this morphology does not result from impurity redistribution.[10,11] In addition, at slightly lower movable heater power levels, solid and liquid Si are found to co-exist within the molten zone. This result can be attributed to the difference in reflectivity between the solid and liquid. It can therefore be concluded that radiative heating plays a major role in determining the shape of the liquid-solid interface under ZMR conditions that yield subboundary-free films.

We believe that the greater difficulty encountered with the conventional ZMR configuration in obtaining subboundary-free 0.5-μm-thick SOI films than in obtaining subboundary-free 1-μm-thick films is explained by the fact that the thinner films absorb less of the incident radiation than the thicker ones, thereby reducing the effect of radiative heating. The relative ease of preparing subboundary-free 0.5-μm-thick films with the new configuration can be attributed principally to an increase in the radiative heating of the crystallizing interface by the movable heater. First, for the same base temperature additional movable heater power is required to melt the SOI film in the new configuration, because the back side of the substrate is no longer heated by the stationary heater. Second, there is a change in the dependence of the molten zone width on movable heater power. In the conventional configuration, a small increase in the movable heater power causes a large increase in the molten zone width. Therefore, the radiative heating at the liquid-solid interface is reduced, because the radiation incident on the interface rapidly decreases with

increasing distance between the interface and the upper heater. This reduction in radiant heating leads to a more nearly planar interface, which results in closely spaced subboundaries in the recrystallized SOI film.[10] In the new configuration, the back side of the substrate is strongly cooled by radiation, enhancing the cooling of the film via thermal conduction through the substrate. Consequently, an increase in the movable heater power leads to a much smaller increase in the molten zone width and therefore to a much smaller decrease in the radiative heating of the crystallizing interface by the upper heater.

It is encouraging that the initial experiments with the new ZMR configuration have yielded such promising results. Many key experimental parameters can be optimized to improve the crystalline quality of SOI films prepared by using this configuration. The radiation intensity profile incident at the crystallizing interface can be adjusted by varying the base temperature of the substrate, changing the shape of the movable heater and the gap between this heater and the sample, and heating or increasing the cooling of the back side of the substrate. Such changes could result in improved surface morphology and reduced wafer warpage. In addition, the radiative spectral output of both the stationary and movable heaters can be shifted by using materials with different emissivities and spectral characteristics. We plan to investigate the effect of using graphite rather than tungsten for the movable heater.

<div style="text-align: right">

C.K. Chen
J.M. Im

</div>

3.2 SELECTIVE PLASMA ETCHING OF Si FROM GaAs-ON-Si WAFERS

The heteroepitaxial growth of device-quality GaAs and GaAlAs layers on Si substrates and the monolithic integration of GaAs-based circuits with Si circuits[12] have generated interest in the possibility of fabricating GaAs microwave integrated circuits in GaAs layers grown on high-resistivity Si substrates. In the past, it has been reported that the resistivity of such substrates was degraded by high-temperature cycling.[13] Because of recent improvements in commercially available float-zone Si, however, the temperatures encountered during GaAs-on-Si growth do not cause any reduction in substrate resistivity. We have reported the fabrication on high-resistivity Si substrates of low-loss transmission lines and GaAs power MESFETs with characteristics comparable to those obtained for components of the same design fabricated on semi-insulating GaAs substrates.[14]

In the course of investigating GaAs-on-Si wafers for microwave applications, we have found that such heteroepitaxial wafers offer an important advantage. In microwave device fabrication, via holes are etched entirely through the substrate, which has been thinned to about 100 μm to obtain 50-Ω microstrip impedance. In processing of homoepitaxial GaAs wafers, the etching process is usually stopped at either the source metallization (for low-inductance grounding) or at the underside of buffer layers (for heat-sinking of power devices). In the second case, etch stop layers such as GaAlAs are included in the device structure but the selectivity obtained for either wet chemical or dry etching is generally inadequate. We have found that CF_4O_2 plasma-etching (~ 1 W/cm^2 at 200 Torr) can be used to etch the Si substrate at rates exceeding 20 μm/h with

112816-17

Figure 3-4. Via hole in GaAs/Si wafer formed by selective plasma etching.

no apparent etching of the GaAs layer. We estimate the etch selectivity of the process to be greater than 10,000:1. By using a thin Ni mask to pattern the back surface of the Si substrate, via holes have been etched completely through the substrate, as illustrated in Figure 3-4. The excellent surface morphology of the exposed GaAs is significantly improved over the morphology generally obtained by selective etching of via holes on GaAs substrates. The gentle slope of the sidewalls has permitted us to obtain uniform gold metallization by using a combination of electroless and electroplating techniques. The extreme etch selectivity that can be obtained for hetero-epitaxial GaAs-on-Si wafers may permit the fabrication of novel device structures.

G.W. Turner   W.L. McGilvary
C.L. Chen   W.F. DeNatale
M.K. Connors   P.M. Nitishin
L.J. Mahoney

REFERENCES

1. *Materials Research Society Symposia Proceedings, Vol. 53*, "Semiconductor-On-Insulator and Thin Film Transistor Technology," edited by A. Chiang, M.W. Geis, and L. Pfeiffer (Materials Research Society, Pittsburgh, Pennsylvania, 1986).

2. *Materials Research Society Symposia Proceedings, Vol. 107*, "Silicon-On-Insulator and Buried Metals in Semiconductors," edited by J.C. Sturm, C.K. Chen, L. Pfeiffer, and L.F. Hemment (Materials Research Society, Pittsburgh, Pennsylvania, 1988).

3. M.W. Geis, H.I. Smith, B-Y. Tsaur, J.C.C. Fan, D.J. Silversmith, and R.W. Mountain, J. Electrochem. Soc. **129**, 2812 (1982), DTIC AD-A154422.

4. M.W. Geis, C.K. Chen, H.I. Smith, P.M. Nitishin, B-Y. Tsaur, and R.W. Mountain, in *Materials Research Society Symposia Proceedings, Vol. 53*, "Semiconductor-On-Insulator and Thin Film Transistor Technology," edited by A. Chiang, M.W. Geis, and L. Pfeiffer (Materials Research Society, Pittsburgh, Pennsylvania, 1986), p. 39, DTIC AD-A174014.

5. L. Pfeiffer, K.W. West, and D.C. Joy, in *Materials Research Society Symposia Proceedings, Vol. 53*, "Semiconductor-On-Insulator and Thin Film Transistor Technology," edited by A. Chiang, M.W. Geis, and L. Pfeiffer (Materials Research Society, Pittsburgh, Pennsylvania, 1986), p. 29.

6. D. Dutartre, in *Materials Research Society Symposia Proceedings, Vol. 107*, "Silicon-On-Insulator and Buried Metals in Semiconductors," edited by J.C. Sturm, C.K. Chen, L. Pfeiffer, and L.F. Hemment (Materials Research Society, Pittsburgh, Pennsylvania, 1988), p. 157.

7. C.K. Chen and J.S. Im, 1988 IEEE SOS/SOI Technology Workshop, St. Simons Island, Georgia, 1-3 October 1988.

8. C.K. Chen, M.W. Geis, M.C. Finn, and B-Y. Tsaur, Appl. Phys. Lett. **48**, 1300 (1986), DTIC AD-A169540.

9. J.S. Im, C.K. Chen, C.V. Thompson, M.W. Geis, and H. Tomita, in *Materials Research Society Symposia Proceedings, Vol. 107*, "Silicon-On-Insulator and Buried Metals in Semiconductors," edited by J.C. Sturm, C.K. Chen, L. Pfeiffer, and L.F. Hemment (Materials Research Society, Pittsburgh, Pennsylvania, 1988), p. 169, DTIC AD-A198006.

10. J.S. Im, C.V. Thompson, and H. Tomita, in *Materials Research Society Symposia Proceedings, Vol. 74*, "Beam-Solid Interactions and Transient Processes," edited by M.O. Thompson, S.T. Picraux, and J.S. Williams (Materials Research Society, Pittsburgh, Pennsylvania, 1987), p. 555.

11. J.S. Im, H. Tomita, and C.V. Thompson, Appl. Phys. Lett. **51**, 685 (1987).

12. *Materials Research Society Symposia Proceedings, Vol. 91*, "Heteroepitaxy on Silicon II," edited by J.M. Phillips and B-Y. Tsaur (Materials Research Society, Pittsburgh, Pennsylvania, 1987).

13. B.W. Battershall and S.D. Emmons, IEEE J. Solid-State Circuits **SC-3**, 107 (1968).

14. G.W. Turner, H.K. Choi, J.P. Mattia, C.L. Chen, S.J. Eglash, and B-Y. Tsaur, in *Materials Research Society Symposia Proceedings*, 1988 Spring Meeting, Reno, Nevada (to be published).

4. SUBMICROMETER TECHNOLOGY

4.1 SELECTIVE-AREA LASER PHOTODEPOSITION OF TRANSPARENT CONDUCTIVE SnO_2 FILMS

The unusual combination of high visible-wavelength transparency and good electrical conductivity has made SnO_2 films important for, among other applications, optoelectronic devices,[1] resistive heating elements,[2] and barrier layers for solar cells.[3] The thin films necessary for such devices can be deposited with the usual sputter, evaporation, and chemical-vapor-deposition techniques,[4] but these require high processing temperatures or post-deposition annealing to obtain the desired properties. We report here on the laser photochemical deposition of SnO_2 to yield highly conductive and transparent thin films of SnO_2. As with other photodeposition processes,[5] selective-area growth can be achieved by patterned surface irradiation.

The chamber used in these experiments was a tainless-steel, six-way cross which could be pumped to a base pressure of a few millitorr using a mechanical pump. The films were deposited using $SnCl_4$ and N_2O as the reactants on room-temperature fused silica substrates which also served as input windows. An ArF excimer laser (193 nm) was the photon source. At 193 nm, $SnCl_4$ undergoes photodissociation via[6]

$$SnCl_4 + h\nu \text{ (6.42 eV)} \rightarrow SnCl_3 + Cl \tag{4-1}$$

with an absorption cross section,[6] in the vapor phase, of 3.8×10^{-17} cm^2. Subsequent photochemical reactions of $SnCl_3$ may strip further Cl atoms from the trichloride radical. N_2O undergoes photodissociation to form N_2 and metastable oxygen:

$$N_2O + h\nu \text{ (6.42 eV)} \rightarrow N_2 + O(^1D) \quad . \tag{4-2}$$

The vapor phase absorption cross section[7] at 193 nm for reaction (4-2) is 7.9×10^{-20} cm^2. We note that both of these vapor reactants adsorb strongly on SiO_2 surfaces, with unknown consequences for the photochemical channels. Initial experiments were performed using 0.75-Torr $SnCl_4$ and 50-Torr N_2O. On the basis of the cross sections, and with the assumption of no fast secondary reactions, the $SnCl_3/O$ photoproduct ratio in the vapor phase is ~7 immediately following each pulse. At fluences approaching ~25 mJ/cm^2 per pulse, essentially all the $SnCl_4$ molecules are dissociated and this ratio drops.

Under these conditions, the photochemical reactions result in two solid products. The first is a moisture-sensitive white powder which collects on all surfaces. Fourier-transform infrared spectroscopy, Auger electron spectroscopy, and solubility analysis reveals this powder to be predominantly $SnOCl_2$. The second product is observed only where the beam irradiates the fused silica surface. It is conductive and, on the basis of evidence below, is identified as primarily SnO_2.

The resistivity and thickness of the SnO_2 films are shown as a function of laser fluence per pulse in Figure 4-1; the laser pulse rate was 5 Hz and the total number of pulses was 10^4. Note that a minimum laser fluence of 10 to 20 mJ/cm^2 per pulse is needed to form conductive SnO_2; below this fluence, only $SnOCl_2$ is formed. At laser fluences greater than 70 to 80 mJ/cm^2 per pulse, ablation of the film is observed and little SnO_2 is deposited.

31
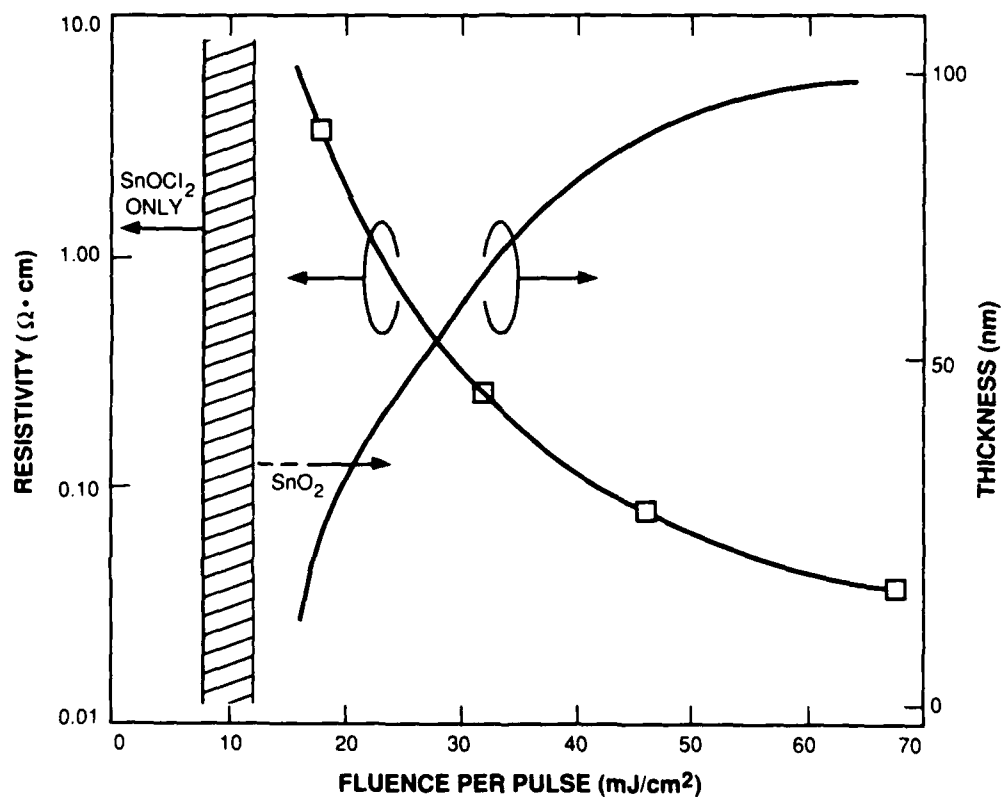
Figure 4-1. Tin oxide film resistivity (left axis) and film thickness (right axis) vs the laser fluence used during growth. For each point, the total number of pulses was fixed at 10^4, the $SnCl_4$ pressure was 0.75 Torr, the N_2O pressure 50 Torr, and the laser pulse rate 5 Hz.
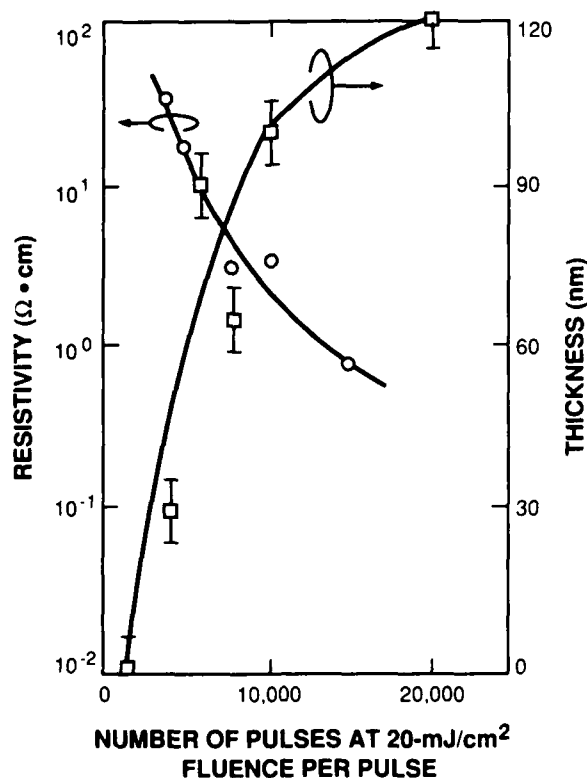
Figure 4-2. Tin oxide film resistivity (left axis) and film thickness (right axis) vs the number of pulses at a constant fluence of 20 mJ/cm^2 per pulse. The gas pressures and laser repetition rate are the same as in Figure 4-1.

Figure 4-2 shows the SnO_2 resistivity and film thickness vs the number of pulses at a laser fluence of 20 mJ/cm^2 per pulse; note that the film thickness begins to saturate with dose at ~100-nm thickness. The 193-nm absorption coefficient of these films was measured to be 1.5×10^5 cm^{-1} (see Figure 4-3), corresponding to an absorption length of 67 nm. From Figure 4-2, the maximum film thickness achievable appears to be approximately two absorption lengths. This is expected since the beam irradiates the reaction volume through the growing film and, hence, film growth slows when the laser irradiation becomes seriously attenuated. A slightly more detailed analysis shows that the reaction rate reduction scales approximately as the Beer's Law attenuation, and is consistent with film growth limited by a photochemical channel dependent linearly on transmitted intensity.

The absorption coefficient of fused silica at 193 nm is of the order 10^{-3} cm^{-1}, whereas those of $SnOCl_2$ and SnO_2 are (by our measurements) 3×10^5 cm^{-1} and 1.5×10^5 cm^{-1}, respectively. As a result, 193-nm substrate absorption is dominantly in an oxychloride adsorbed layer even at submonolayer thickness. The temperature rise due to the laser pulse depends strongly on the condensed-layer thickness. If we assume for the moment that the dominant absorbing layer is

33
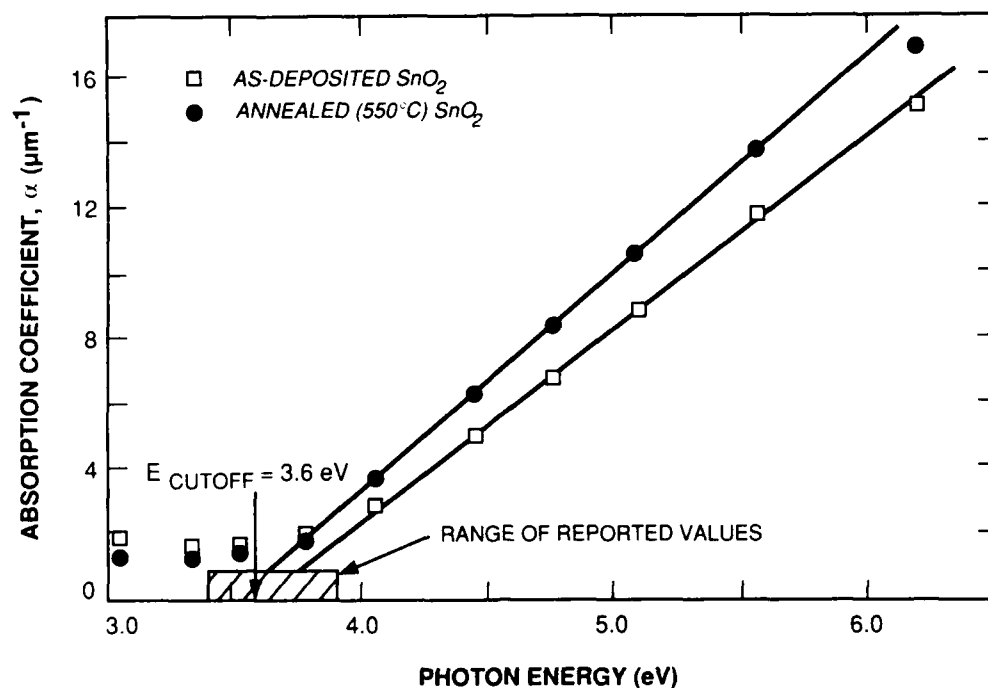
Figure 4-3. Optical absorption coefficient vs photon energy of an as-deposited tin oxide film (squares) and an annealed (550° C, 2 h, in air) film.

$SnOCl_2$, calculation of the temperature rise indicates that the maximum temperature during the laser pulse is less than 150°C for $SnOCl_2$ layers less than 4 nm thick. The thermal conversion to the oxide cannot occur at these thicknesses since $SnOCl_2$ thermally decomposes into SnO_2 only at temperatures greater than 150°C (Reference 8). However, a photochemical conversion is not ruled out. Once the growing oxychloride film becomes thick enough to absorb a significant portion of the laser energy, the laser-induced temperature rise can exceed 150°C and the formation of SnO_2 can proceed via a thermally activated mechanism. Thermal analysis places an upper bound of 300° to 400°C on the peak laser-induced temperature of a fully attenuating film at the maximum laser power of the experiment.

Some element of thermal reaction appears to be essential to achieve good material properties since, when low fluence laser pulses are used, the films never acquire low values of resistivity (see Figure 4-1). The nature of this mechanism is unclear, but may involve outdiffusion of chlorine, recrystallization, or subtle changes in stoichiometry. However, it does not appear to depend upon vapor-phase formation of oxygen atoms, as is thought to be the case for UV photochemical annealing of tantalum oxide.[9] Several samples of SnO_2 were prepared using only 5×10^3 pulses at 20 mJ/cm^2 per pulse (see Figure 4-2). The samples were then irradiated with another 10^4 pulses, one sample in 500-Torr helium, another in 500-Torr N_2O. In spite of the efficient generation of oxygen atoms in the latter case, the resulting resistivities for the two ambients were virtually identical (0.57 ohm-cm).

34

The data of Figure 4-3 for the optical absorption coefficient of a laser-deposited film vs photon energy show a cutoff energy of 3.6 eV (340 nm), well within the range of good films deposited by other means. Also shown in Figure 4-3 is a curve for the same film after annealing. Heating to 550°C for 2 h in air is a fairly common post-deposition treatment to maximize the conductivity[10] of conventionally deposited SnO_2 films. It is interesting to note that this anneal has little effect on either the optical absorption or the resistivity of the laser photodeposited films. By plotting these data in a fashion similar to Spence,[11] the band gap was determined to be 3.2 eV for the as-deposited film and 3.1 eV for the annealed film. Each is quite close to the reported value of 3.54 eV for pure, crystalline SnO_2. Auger spectroscopy showed undetectable (less than 1 percent) chlorine in the as-deposited film. Although the actual concentration of chlorine was not measured, its presence at less than 1-percent levels could affect the electrical properties of the films.[12]

Since the formation of the SnO_2 requires laser irradiation on the surface, selective-area deposition of thin, conductive lines was possible. Lines 10 μm wide of SnO_2 have been deposited by proximity printing through a mask. Well-delineated smooth films are formed. Small nuclei of $SnOCl_2$, nucleated in the vapor, can be observed between the SnO_2 lines. This type of selective-area patterning, using optical imaging or scanned focused beams, has application in such processes as electrode repair on electroluminescent display panels and solar cells.

In summary, selective-area photodeposition of SnO_2 with resistivities as low as 0.04 ohm-cm has been demonstrated with an ArF excimer laser. Based on previous studies, even lower resistivities may be possible through the incorporation of dopants such as indium, antimony, or fluorine during film growth. The mechanism for the film formation is thought to be through the photochemically activated vapor-phase reaction of $SnCl_4$ and N_2O to form $SnOCl_2$. The SnO_2 is grown via the decomposition of thin layers of the $SnOCl_2$ that accumulate between laser pulses. The transient (20-ns-duration) temperature of the surface does not exceed 300° to 400°C throughout the film growth and does not penetrate significantly into the substrate. The optical band gap of 3.2 eV and transmission cutoff wavelength of 340 nm compare favorably with films deposited by other means.

<div style="text-align:right">

R.R. Kunz
M. Rothschild
D.J. Ehrlich

</div>

4.2 ELECTRICAL CHARACTERISTICS OF ULTRASHALLOW-JUNCTION DIODES FABRICATED BY LASER DOPING

Shallow source/drain junctions are required to reduce short-channel effects for submicrometer MOSFETs, but it is becoming increasingly difficult to fabricate them by conventional ion-implantation technology, particularly for p^+-n junctions. The process of using a pulsed XeCl excimer laser (λ = 308 nm) with B_2H_6 or BF_3 gas as a dopant source to form very shallow p^+ doped regions in silicon has been investigated with promising results.[13,14] In the work described here, we have used a pulsed ArF excimer laser (λ = 193 nm) and a BCl_3 ambient to fabricate
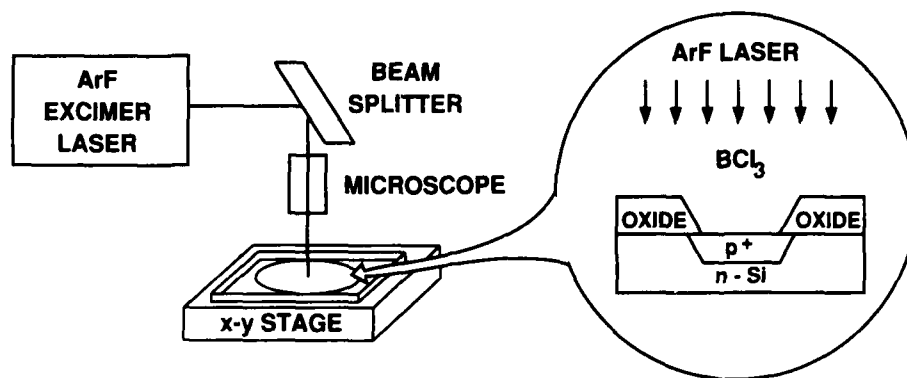
Figure 4-4.   Schematic diagram of the laser-doping setup and of a diode test structure.
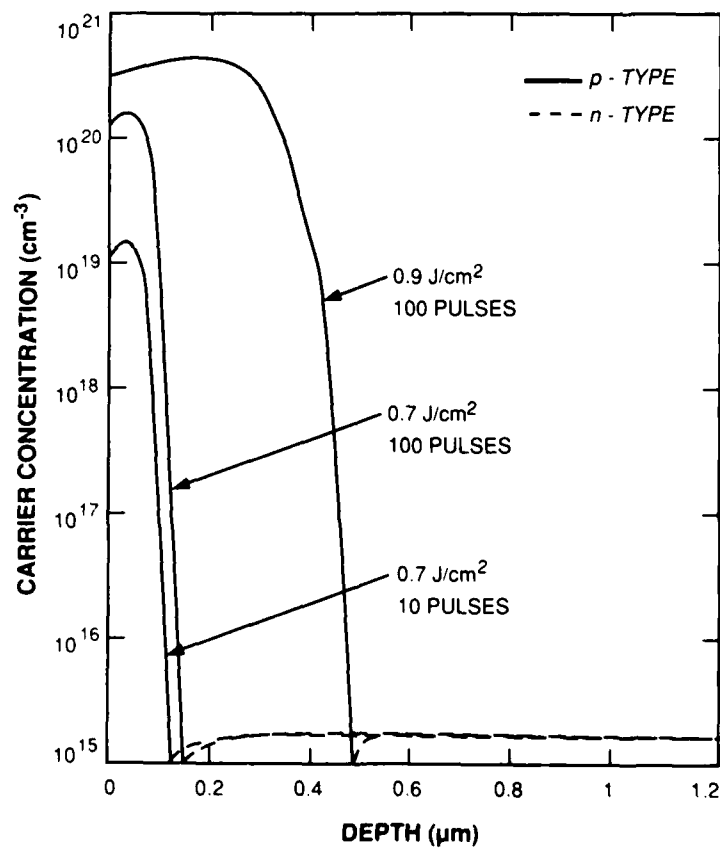
Figure 4-5.   Profile of activated boron concentration in laser-doped diodes, obtained by spreading-resistance measurement.

shallow p^+-n junction diodes, and we have studied the dependence of the diode characteristics on laser-doping conditions.

The schematic diagram of the laser-doping setup is shown in Figure 4-4. Silicon dioxide was first grown on 3-in n-type silicon wafers and then etched to form a hole pattern which exposed the silicon surface for laser doping. The ArF excimer laser was used as an energy source to cause photodissociation of BCl_3 and to melt the silicon surface. After laser doping, aluminum was sputter deposited, patterned, and sintered in forming gas at 380°C to form the Al-p^+-n diode structure. For our ArF excimer laser, the pulse duration is fixed at about 20 ns (FWHM).

Figure 4-5 shows the activated boron profile, measured by the spreading-resistance method, under various laser-doping conditions. The threshold energy density incident on the silicon which will produce melting is about 0.6 J/cm^2 for our ArF laser, which is slightly lower than the melting threshold of 0.7 J/cm^2 predicted by the LASERMELT simulation[15] for a XeCl laser. According to the LASERMELT simulation, the junction depth increases with both the number of laser pulses and the silicon melt depth during the pulse, which in turn increases with the laser pulse energy. For laser doping with an energy density of 0.9 J/cm^2 per pulse, the junction depth is about 0.5 μm after 100 pulses and the silicon surface becomes rough because of laser damage. For an energy density of 0.7 J/cm^2 per pulse, the melt depth is shallower and the junction depth becomes less sensitive to the number of pulses. As shown in Figure 4-5, a 0.1- to 0.15-μm junction depth was obtained at an energy density per pulse of 0.7 J/cm^2. No damage was observed on the silicon surface when the energy density per pulse is at or below 0.7 J/cm^2.

The electrical characteristics of laser-doped junction diodes depend on the laser pulse energy and the number of pulses. Figure 4-6 shows the I-V characteristics of laser-doped diodes exposed to 150 pulses at various energy densities per pulse. By comparing the laser-doped diodes with Al/n-Si Schottky-diode characteristics [curve (d) in Figure 4-6], we found that the incorporation of a p^+ layer by laser doping increased the barrier height and lowered the forward-bias current.
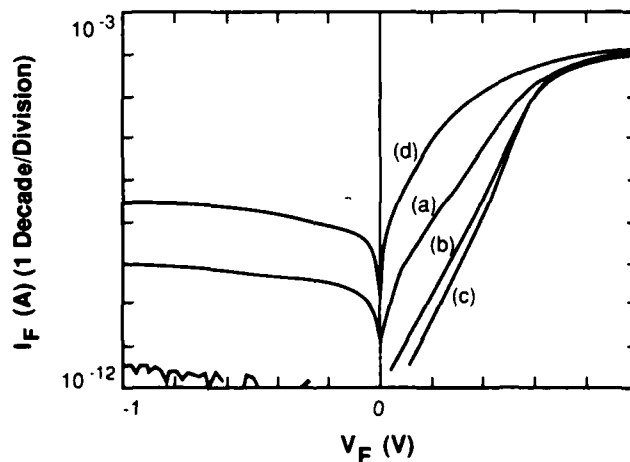

Figure 4-6.   Current-voltage characteristics of various laser-doped p^+-n junction diodes exposed to 150 pulses at energy densities per pulse of (a) 1.1 J/cm^2, (b) 0.9 J/cm^2, and (c) 0.7 J/cm^2. Curve (d) is for an Al/n-Si Schottky reference diode.

37

The diode ideality factor decreases to 1 with increasing energy density, and then increases with higher laser energy. The high ideality factor for diodes doped at high laser energy can be attributed to the surface damage. Figure 4-7 plots the diode ideality factor vs number of laser pulses with energy density as a parameter. At the optimum energy density of 0.7 J/cm^2 per pulse, the diode characteristics become independent of number of pulses for more than 30 pulses.
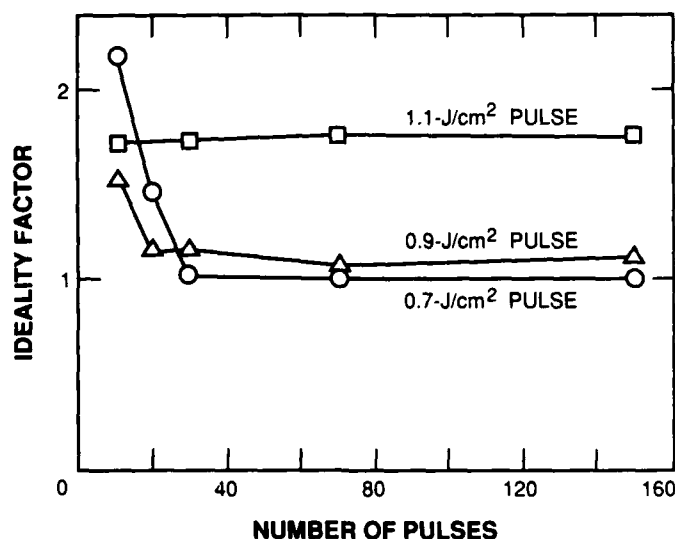
Figure 4-7.   Plot of the ideality factor of laser-doped diodes against the number of pulses during laser doping with energy density per pulse as a parameter.

The reverse-bias I-V characteristic of a laser-doped diode is shown in Figure 4-8. The breakdown voltage is above 40 V, much higher than that of an Al/n-Si Schottky diode. The dependence of reverse-bias current on laser-doping conditions is generally consistent with forward-bias

Figure 4-8.   Reverse-bias current-voltage characteristics of (a) a laser-doped p$^+$-n junction diode with energy density per pulse of 0.7 J/cm^2 and 50 pulses, and of (b) an Al/n-Si Schottky diode as reference.
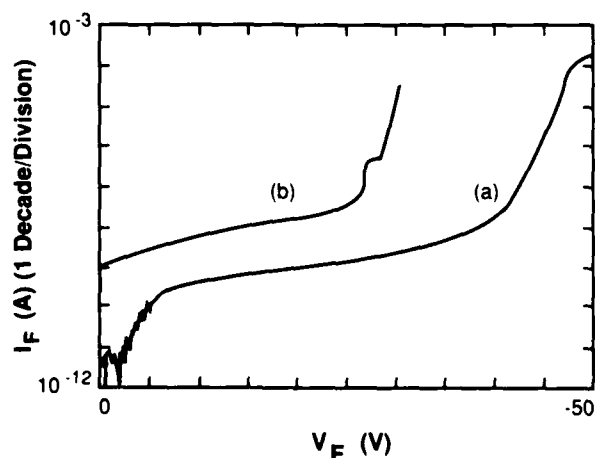
38
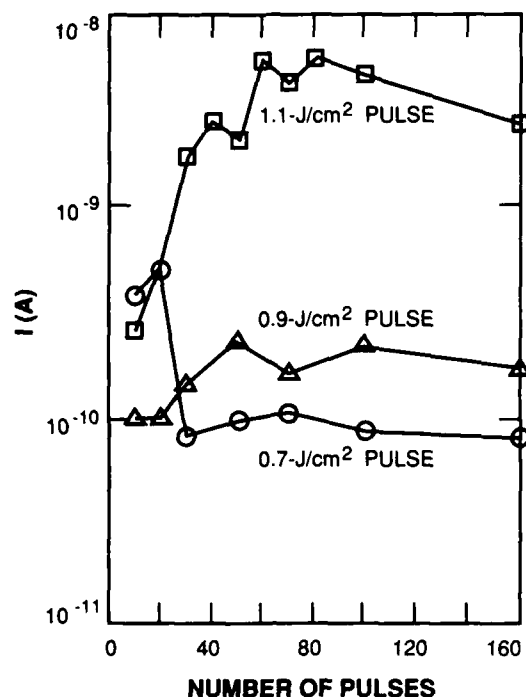
Figure 4-9. Plot of the reverse leakage current at $V_{bias} = 5$ V for the laser-doped diodes against the number of pulses during laser doping with the energy density per pulse as a parameter.

results. As illustrated in Figure 4-9, the lowest leakage currents were observed for the diodes doped with an energy density of 0.7 J/cm^2 per pulse, and leakage was almost independent of the number of pulses for more than 30 pulses.

In summary, ultrashallow-junction p^+-n diodes have been fabricated with ArF laser doping. The junction depth increases with energy density and the number of pulses. Excellent diode characteristics have been obtained with a junction depth of about 0.1 μm.

K.K. Young   D.C. Shaver
M. Rothschild   D.J. Ehrlich
T.J. Pack

4.3   PATTERNED EXCIMER-LASER ETCHING OF GaAs WITHIN A MOLECULAR BEAM EPITAXY MACHINE

The present trend of integrating optical and electronic devices on single chips requires the sequential overlaying of patterned layers to produce three-dimensionally structured materials. For III-V compounds, surface oxidation and impurity contamination are factors which make less desirable normal processing of thin layers in multiple steps involving air exposure. Here, we describe an *in situ* excimer-laser-patterned projection etching process used on a molecular beam epitaxy machine which demonstrates the basic processing steps required for 3-D structures in GaAs.

The system has two ultrahigh-vacuum chambers which are isolated by a gate valve. In one chamber, GaAs is grown by elemental-source molecular beam epitaxy. In the second chamber, chlorine gas is introduced through a leak valve, and the sample is exposed to an ArF excimer laser (193 nm) through a single-element optical projection system. Samples are transferred between the two chambers under ultrahigh-vacuum conditions.

We have examined the dependence of the etching rate on pulse repetition rate (PRR), chlorine pressure, and pulse energy density (fluence). Figure 4-10 shows the dependence of the etch rate per pulse on the PRR at a chlorine pressure of 5×10^{-3} Torr. The data below 0.5 pps were taken at a fluence of 10 mJ/cm^2, while the data above 0.5 pps were taken at a slightly lower fluence ($\sim$8 mJ/cm^2). Three different repetition-rate dependences are apparent which result from the progress of the GaAs/chlorine reaction at the instant of laser-pulse exposure. Studies[16-18] have suggested that molecular chlorine reacts with GaAs first through a fast reaction which forms products of monochlorides or dichlorides of arsenic and gallium on the surface, followed by a slower reaction which forms trichlorides. As the trichloride products build up, the surface becomes covered predominantly with gallium trichloride. This results since the more volatile arsenic trichloride tends to evaporate rapidly. In the steady state, the etch rate is limited by the evaporation of gallium trichloride from the surface, which is required in order to provide new sites for the reaction to occur.[18] At room temperature, the evaporation rate is quite low. We postulate that the role of the laser pulse is to desorb the reaction products from the surface, so that the reaction proceeds anew between pulses. The etch rate/pulse saturation below 0.5 pps results from the reaction slowing as a full monolayer coverage of gallium trichloride is obtained. The
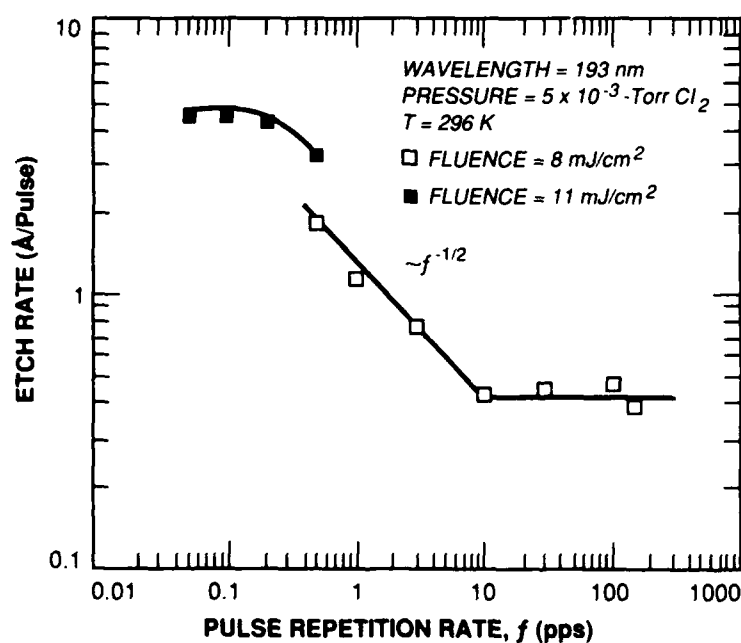

Figure 4-10. Dependence of the etch rate per pulse on the pulse repetition rate at a chlorine pressure of 5×10^{-3} Torr and a fluence of $\leq$11 mJ/cm^2.

40

exact etch rate at saturation depends on the fluence, as will be discussed below. Between 0.5 and 10 pps, the etch rate follows an inverse square-root dependence on the PRR. This corresponds to a square root of time dependence for product formation, and suggests a diffusion-limited step in the reaction. Above 10 pps, the etch rate/pulse is again constant, as the slow-reaction products do not have sufficient time between pulses to build up, and the initial fast reaction has already reached completion.

The dependence of the etch rate/pulse on the fluence is shown in Figure 4-11. The data at 0.5 pps probe the slow reaction, while the data at 25 pps probe the fast reaction. The saturation observed at 15 mJ/cm^2 for both PRRs occurs as the laser pulse desorbs all the reaction products from the surface. Above 18 mJ/cm^2, a deterioration of the surface morphology is observed, which indicates a transition to a thermal damage mechanism. The etch rate saturates at 4.4 Å per pulse for 0.5 pps, which from Figure 4-10 is just below the pulse period saturation. We speculate that the layer thickness consumed by the reaction in the long-time limit may approach 5.6 Å per pulse, which would correspond to a GaAs removal rate of two monolayers/pulse, or a monolayer coverage of gallium trichloride. We note that controlled removal of GaAs bilayers would be useful for *in-situ* processing of quantum-well structures. At 25 pps, the saturation at 1.6 Å/pulse indicates that the fast reaction is controlled by only a limited number of sites on the surface.
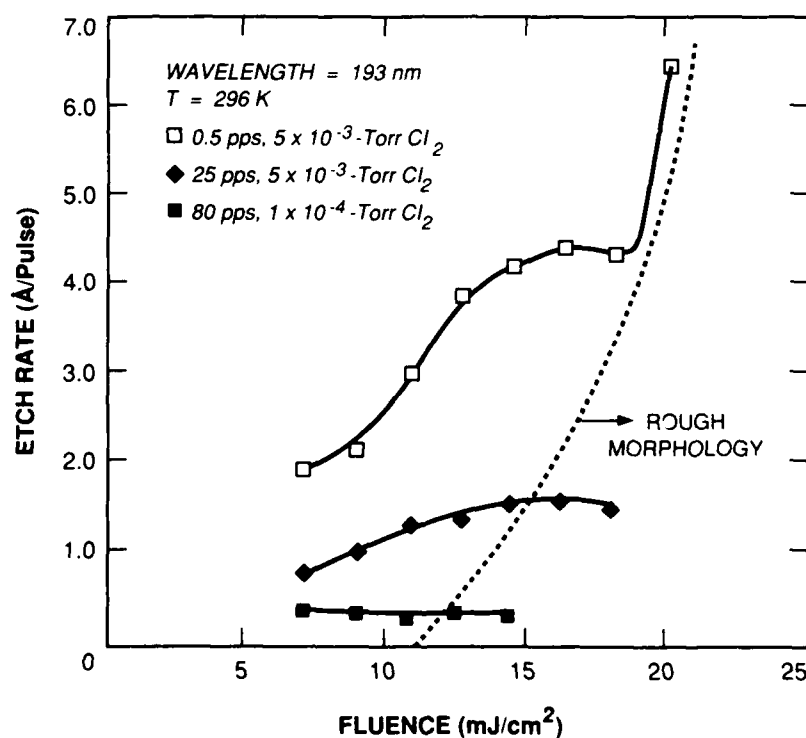
Figure 4-11. Dependence of the etch rate per pulse on the fluence at a repetition rate of 0.5 and 25 pps and a chlorine pressure of 5 × 10^{-3} Torr, and 80 pps at a chlorine pressure of 10^{-4} Torr. Approximate boundary of the transition from a smooth surface to a rough surface is indicated.
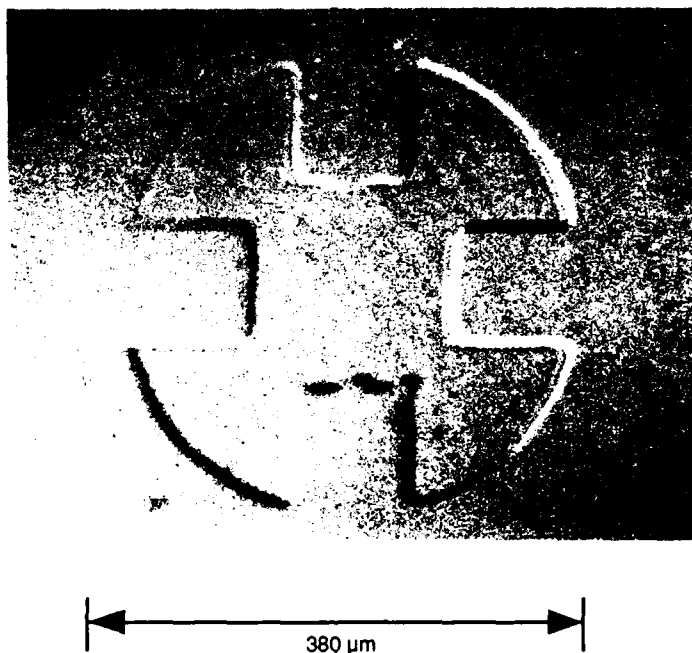
41

380 μm

Figure 4-12. Optical micrograph of an etched and overgrown epitaxial film of GaAs. Etched region is the interior of the cloverleaf pattern.

42

The dependence of the etching process on chlorine pressure is governed largely by the monolayer arrival rate of chlorine relative to the PRR. If the monolayer arrival rate is much greater than the PRR, then the etch rate is only weakly dependent on the chlorine pressure in the range of 10^{-4} to 5×10^{-3} Torr. If the chlorine arrival rate is less than the PRR, then the etch rate is limited by chlorine arrival and becomes constant in time. At 10^{-4} Torr, this occurs above 60 pps.

Figure 4-12 shows an optical micrograph of a GaAs surface after a complete growth, etching, and overgrowth sequence. The pattern was projected onto the surface using a mask and a lens external to the etching chamber. The sequence of steps was a growth of a 0.5-μm thickness of GaAs, followed by etching of 0.1 μm, and then overgrowth with 0.3 μm of GaAs. The interior of the cloverleaf pattern is the etched area. The etch parameters were 0.5 pps, 5×10^{-3} Torr of Cl_2, and a fluence below saturation. The ripple observed on the surface results from spatial inhomogeneities in the laser pulse fluence. This can be avoided by an improved optical system, etching at fluence saturation, or etching under conditions where the rate is limited by chlorine arrival.

This work demonstrates a controllable etch process which can be used *in situ* to etch patterns in GaAs. At present, the resolution of the etching process is limited by the optical system and movement of the sample mount. Significant improvements in the resolution are likely. Preliminary studies suggest that this work may be extended to other III-V materials, such that *in situ* processing of heterostructures is possible.

P.A. Maki
D.J. Ehrlich

43

REFERENCES

1. H. Iida, N. Shibata, T. Mishuku, A. Ito, H. Karasawa, and Y. Hayashi, IEEE Electron Device Lett. **EDL-4**, 157 (1983).

2. C. Mellor and K.A. Petersen, U.S. Patent Applied Docket No. 85-1-153 (September 1987).

3. D.K. Schroder, IEEE Trans. Electron Devices **ED-25**, 90 (1978).

4. J.C. Manifacier, Thin Solid Films **90**, 297 (1982).

5. A review may be found in *Laser Microfabrication: Thin-Film Processes and Lithography*, D.J. Ehrlich and J.Y. Tsao, Eds. (Academic Press, Boston, 1989).

6. J. Fernandez, G. Lespes, and A. Dargelos, Chem. Phys. **111**, 97 (1987).

7. C. Hubrich and F. Stahl, J. Photochem. **12**, 93 (1980).

8. S.S. Batsanov and N.A. Shestakova, Izv. Akad. Nauk SSSR, Neorg. Mater. [Inorg. Mater.(USSR)] **2**, 110 (1966).

9. M. Matsui, S. Oka, K. Yamegishi, K. Kuroiwa, and Y. Tarui, Jpn. J. Appl. Phys. **27**, 506 (1988).

10. R. Banerjee and D. Das, Thin Solid Films **149**, 291 (1987).

11. W. Spence, J. Appl. Phys. **38**, 3767 (1967).

12. J.A. Aboaf, V.C. Marcotte, and N.J. Chou, J. Electrochem. Soc. **120**, 701 (1973).

13. P.G. Carey, K.H. Weiner, and T.W. Sigmon, IEEE Electron Device Lett. **EDL-9**, 542 (1988).

14. P.G. Carey, T.W. Sigmon, R.L. Press, and T.S. Fahlen, IEEE Electron Device Lett. **EDL-6**, 241 (1985).

15. E. Landi, P.G. Carey, and T.W. Sigmon, IEEE Trans. Computer-Aided Design **CAD-7**, 205 (1988).

16. M. Balooch, D.R. Olander, and W.J. Siekhaus, J. Vac. Sci. Technol. B **4**, 794 (1986).

17. M.S. Ameen and T.M. Mayer, J. Appl. Phys. **63**, 1152 (1988)

18. J.H. Ha, E.A. Ogryzlo, and S. Polyhronopoulos, J. Chem. Phys. **89**, 2844 (1988)

5. MICROELECTRONICS

5.1 PBT AMPLIFICATION AT 94 GHz

We report the first measurement of small-signal gain for a GaAs permeable-base-transistor (PBT) amplifier operating at 94 GHz. The PBT[1] is a vertical-current-flow transistor whose control electrode is a grid of tungsten epitaxially overgrown with GaAs. All previous measurements of the PBT have been at or below 50 GHz (see References 2 through 4).

A scalar network analyzer[5] covering the 90-to-97-GHz frequency band was assembled using an IMPATT-diode swept-frequency source, WR-10 waveguide components, and a receiver/data normalizer. Transmission and reflection measurements were made on a PBT mounted in a 94-GHz test fixture.

The test fixture (Figure 5-1) includes two transitions from WR-10 waveguide to 50-Ω microstrip. Each transition is realized using an extension of the microstrip as an E-plane waveguide probe. The PBT is mounted on the narrow edge of a 250-μm-thick metal carrier. The carrier is put between the two back-to-back waveguide-to-microstrip transitions, and the PBT is connected to the microstrip lines with gold mesh.

A: PBT CARRIER
B: WAVEGUIDE SHORT
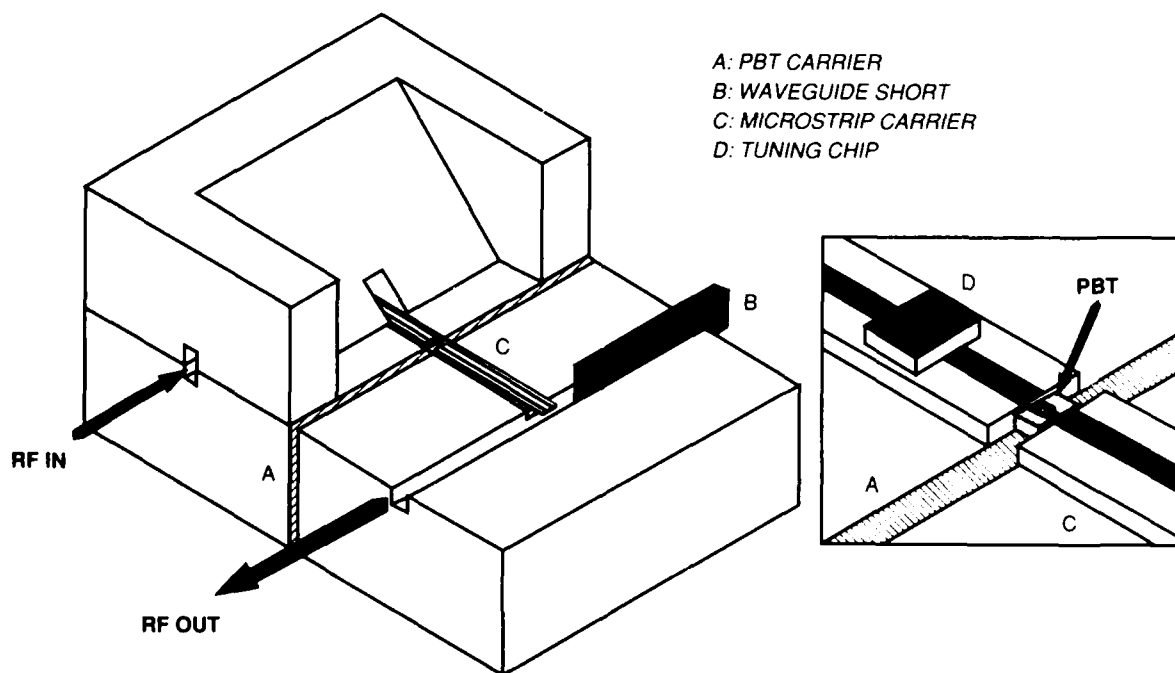C: MICROSTRIP CARRIER
D: TUNING CHIP

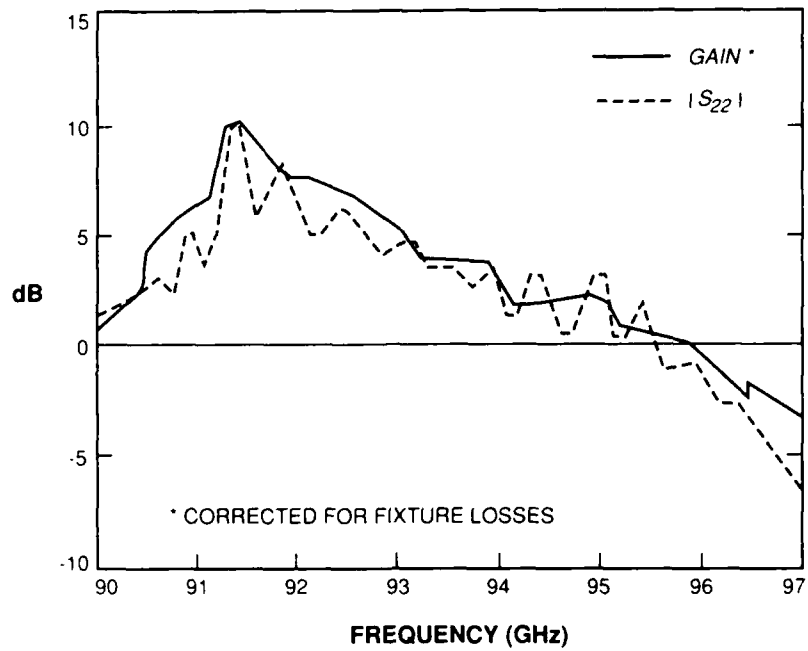Figure 5-1. 94-GHz test fixture.

45

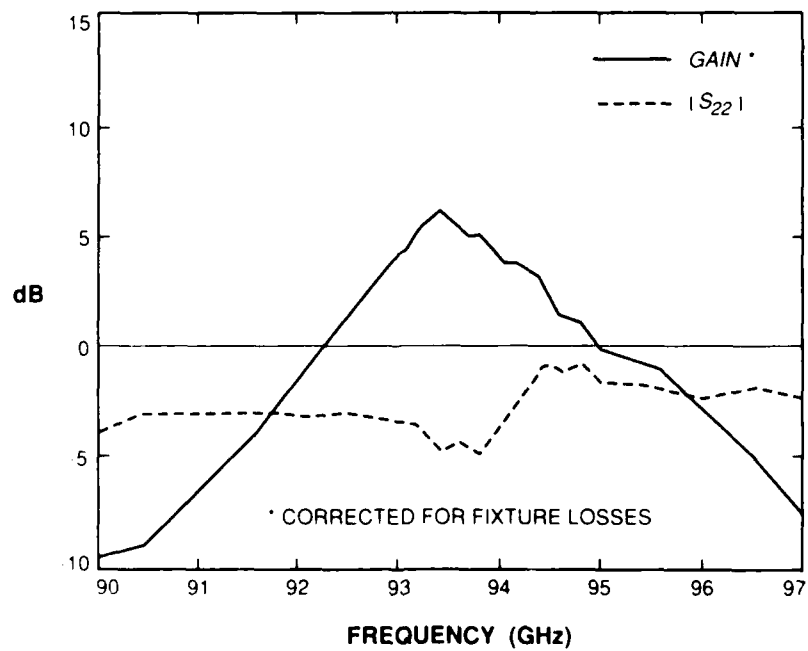*Figure 5-2. PBT single-stage hybrid amplifier: regenerative tuning.*

Figure 5-3. PBT single-stage hybrid amplifier: non-regenerative tuning.

46

The PBT was tuned empirically by placing metallized alumina chips on the microstrip line to vary the impedance. The tuning and bias were adjusted to maximize the gain at a frequency within the measurement band and to minimize the magnitude of either the fixture input or output reflection coefficient. Fixture losses, which were used to correct the gain data, were obtained from a through-line measurement.

Results of the measurements are shown in Figures 5-2 and 5-3. Device gain and the magnitude of the fixture output reflection coefficient $|S_{22}|$ are plotted as a function of frequency for two different sets of tuning and bias conditions. In Figure 5-2, the maximum device gain was 10 dB at 91.4 GHz with an associated $|S_{22}|$ of 10 dB. While this gain is the highest reported for any transistor at these frequencies, $|S_{22}|$ greater than 0 dB indicates that the amplifier had positive feedback. Figure 5-3 shows the results for a second set of tuning and bias conditions. At 93.4 GHz, the maximum device gain was 6 dB and $|S_{22}|$ is less than 0 dB, showing no positive feedback under these conditions.

The PBT, like all active devices, has parasitic circuit elements which create internal feedback paths. The nature of the internal feedback depends on the terminating impedances and on device parameters, some of which vary with bias. Operating with positive feedback increases the gain but also the noise, requiring performance trade-offs to be made in an amplifier design. These preliminary results demonstrate the PBT's ability to provide significant gain either with or without positive internal feedback. Since gain is difficult to achieve at 94 GHz, the ability to povide high gain, even with positive internal feedback, may prove to be an asset for the PBT.

R.H. Mathews R.A. Murphy
R. Actis   K.B. Nichols
B.J. Clifton   C.O. Bozler
M.A. Hollis

5.2 A 64 × 64-PIXEL BACK-ILLUMINATED CCD IMAGER WITH LOW NOISE AND HIGH FRAME RATES

Devices which are capable of recording events involving small numbers of photons on a time scale of the order of that for atmospheric turbulence (~ 1 ms) are required for sensor applications in adaptive optics and speckle imaging. This report describes a 64 × 64-pixel frame-transfer charge-coupled device (CCD) fabricated for such low-noise, high-frame-rate, and high-quantum-efficiency applications. A significant achievement of this sensor is a measured equivalent noise signal of 20 electrons rms over a 5.5-MHz bandwidth at 25°C.

Figure 5-4 describes the architecture of the imager. The device uses a buried-channel, three-phase, triple-polysilicon process with 27 × 27-μm pixels. The incoming light is integrated in the 64 × 64-pixel imaging array and then is rapidly transferred to the 64 × 64-pixel frame-store array. The transfer is done quickly (<17 μs) to minimize image smear. An electronic shutter has been implemented by adding an n^+ diode along the top of the imaging array. This feature enables fast disposal of unwanted photocarriers generated in the imaging array and avoids their transfer
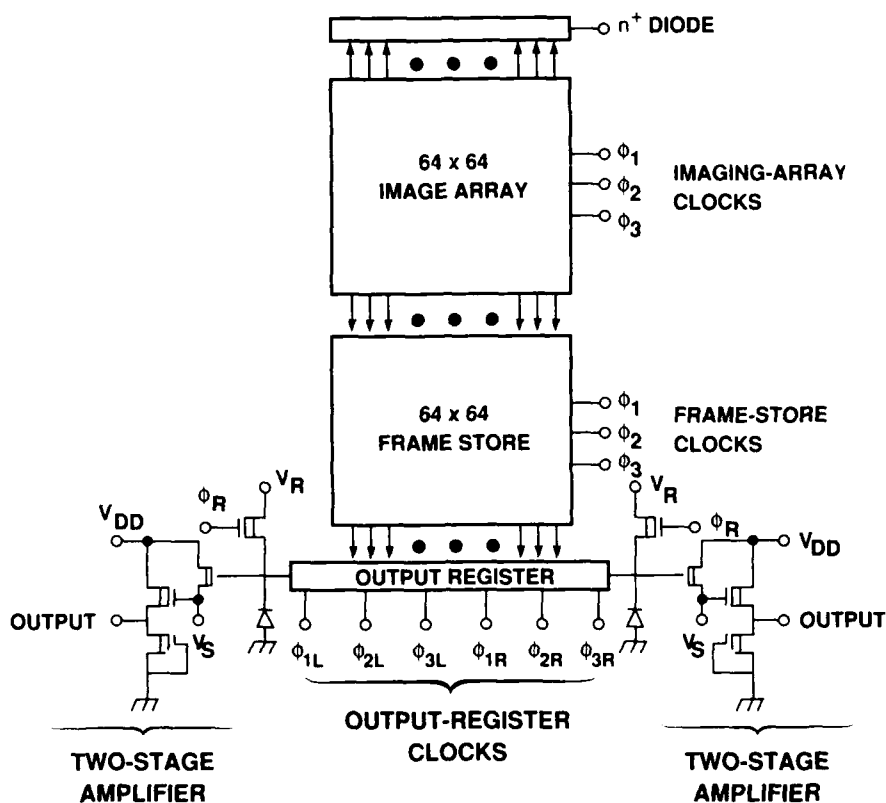
Figure 5-4. Schematic diagram of 64 × 64-pixel frame-transfer CCD imager.

through the frame-store array. Output amplifiers are symmetrically located on both sides of the serial output register. The output register can be clocked so that half of the pixels are directed to each of the two outputs, or all the pixels are directed to either output. A rate of 2000 frames per second is achieved by simultaneous clocking of the two outputs. The output circuit is a two-stage source-follower optimized for low noise.

The key to the low-noise performance is the use of buried-channel FETs, the minimization of parasitic capacitances, and the use of resistive loads instead of generally noisier FET current sources. A 10-μm-wide, 2-μm-long buried-channel transistor is used as the active transistor of the first-stage source-follower to obtain low 1/f noise. The drain diffusion is offset 2 μm from the gate edge to minimize the gate-drain (Miller) capacitance while having negligible effect on the transistor gain. Measured values of the Miller capacitance are approximately 0.1 fF/μm for this structure. Figure 5-5 illustrates a cross section of this transistor. A 3 × 3-μm buried contact connects the floating diffusion sense node directly to the gate polysilicon of the first-stage source-follower transistor. The buried contact structure minimizes the area and, thus, capacitance associated with the sense node. Measured values of responsivity are as high as 12 μV/electron, corresponding to an equivalent sense node capacitance of 10 fF.
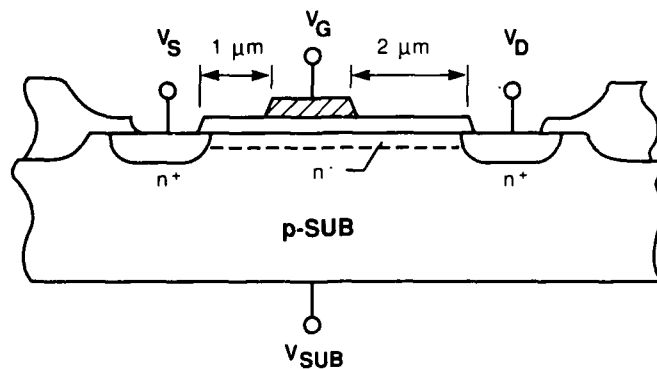
48

*Figure 5-5.   Cross section of the first-stage source-follower with drain
diffusion offset 2 μm from gate edge.*

Back-illumination is an essential requirement for this application for two reasons. First,
back-illumination maximizes quantum efficiency by giving essentially a 100-percent fill factor for
photon capture and providing a planar surface for straightforward application of antireflection
coatings to minimize reflection losses. Second, the response of the device to a point source of
light scanned over a pixel is a smooth function of position. This is a requirement for wavefront
sensors such as the Hartman sensor.[6] Back-illuminated versions of the imager have been fabri-
cated and optimized for high quantum efficiency around 500 nm. Figure 5-6 is a photograph of
a packaged back-illuminated CCD imager.

R.K. Reich   J.H. Reinold
B.E. Burke   C.L. Doherty
W.H. McGonagle   C.M. Huang
R.W. Mountain   B.W. Johnson
G.A. Lincoln

5.3 HIGH-SPEED RESONANT-TUNNELING DIODES MADE FROM THE PSEUDOMORPHIC $In_{0.53}Ga_{0.47}As/AlAs$ SYSTEM

We report here the successful growth and first high-frequency demonstration of resonant-
tunneling diodes consisting of two 6-monolayer-thick AlAs barriers and an 8-monolayer-thick
$In_{0.53}Ga_{0.47}As$ quantum well. As shown in Figure 5-7, the cathode and anode regions outside the
barriers were also $In_{0.53}Ga_{0.47}As$ lattice-matched to the InP substrate. The AlAs barriers are
strained because of the lattice mismatch between InGaAs and AlAs (lattice constants of 0.587
and 0.567 nm, respectively), but the barrier thickness is far too small for the formation of dislo-
cations. The layers were grown by molecular beam epitaxy on n^+-InP (100) substrates at a
growth temperature of 470°C. Lightly doped ($N_D = 2 \times 10^{16}$ cm^{-3}) buffer layers were grown out-
side of each barrier to insure against the diffusion of dopant into the barriers during growth.
Mesa isolation was accomplished by wet chemical etching. This combination of InGaAs/
AlAs/InGaAs heterobarriers and buffer layers yields peak-to-valley ratios of 28:1 at 295 K and
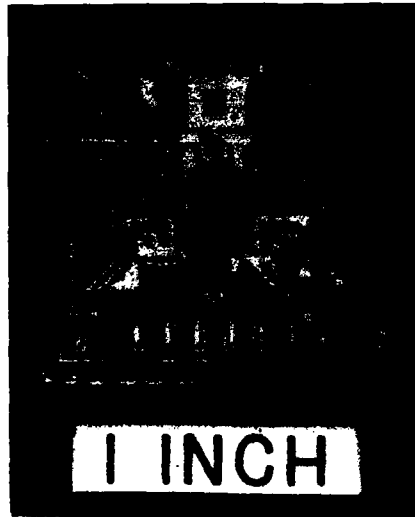
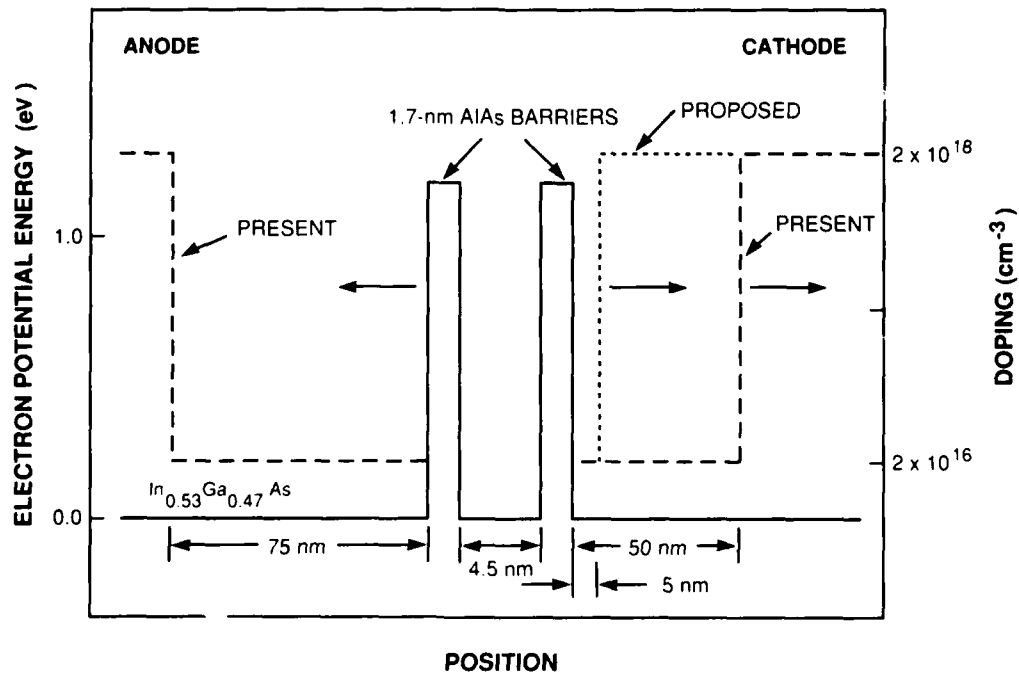*Figure 5-6.   Photograph of a packaged back-illuminated 64 × 64-pixel CCD imager.*

Figure 5-7.   Composition and doping profiles for the present and proposed InGaAs/AlAs resonant-tunneling diodes.

70:1 at 77 K. The peak current density at room temperature, $J_P = 8 \times 10^3$ A cm^{-2}, is approximately one-half of the value predicted by coherent resonant-tunneling theory (Figure 5-8), while the valley current density (Figure 5-9) exceeds the theoretical value by a factor of 8 at room temperature and a factor of 7 at 77 K. This valley current factor may be compared with a factor of ~ 100 discrepancy at both temperatures for devices made from the GaAs/AlGaAs system.

To test the speed of these devices, they were mounted in a series of microwave resonators. At 0.3 GHz, an 8-μm-diam. device generated a power of 330 μW, which is 75 percent of the theoretical maximum level. As shown in Figure 5-10, the power decreased rapidly above about 13 GHz, and no fundamental oscillations could be observed above 28 GHz. These power data are explained by a simple RC circuit model of the device containing a relatively large series resistance. Separate network analyzer measurements determined the specific series resistance to be $R_s \sim 1.5 \times 10^{-5}$ $\Omega \cdot$ cm^2. This resistance may arise from poor ohmic contacts or from the InGaAs/InP heterojunction, which has a conduction-band offset of about 0.3 eV. Calculations indicate that oscillations up to at least 600 GHz should be attainable by decreasing the thickness of the buffer layer on the cathode side (to increase the current density) as proposed in Figure 5-7, and by increasing the doping concentration in the epilayers adjacent to the substrate and top contact (to reduce the series resistance). In this estimate, we have assumed an overall specific resistance of 1×10^{-7} $\Omega \cdot$ cm^2. These results suggest that the InGaAs/AlAs system is superior to the GaAs/AlGaAs system for most foreseeable resonant-tunneling applications.

E.R. Brown   T.C.L.G. Sollner

A.R. Calawa   C.L. Chen

M.J. Manfra   C.D. Parker

REFERENCES

1.   C.O. Bozler and G.D. Alley, IEEE Trans. Electron Devices **ED-27**, 1128 (1980), DTIC AD-A096619.

2.   C.O. Bozler, M.A. Hollis, K.B. Nichols, S. Rabe, A. Vera, and C.L. Chen, IEEE Electron Device Lett. **EDL-6**, 456 (1985).

3.   L.J. Kushner, M.A. Hollis, R.H. Mathews, K.B. Nichols, and C.O. Bozler, 1988 IEEE Int. Microwave Symp. Digest, 25-27 May 1988, p. 525, DTIC AD-A194631.

4.   R. Actis, R.W. Chick, M.A. Hollis, B.J. Clifton, K.B. Nichols, and C.O. Bozler, IEEE Electron Device Lett. **EDL-8**, 66 (1987).

5.   J.B. Knorr, IEEE Trans. Microwave Theory Tech. **MTT-32**, 183 (1984).

6   J.C. Wyant and C.L. Koliopoulos, Special Topics in Optical Propagation, 28th Meeting of Electromagnetic Wave Propagation Panel, p. 300 (1981).

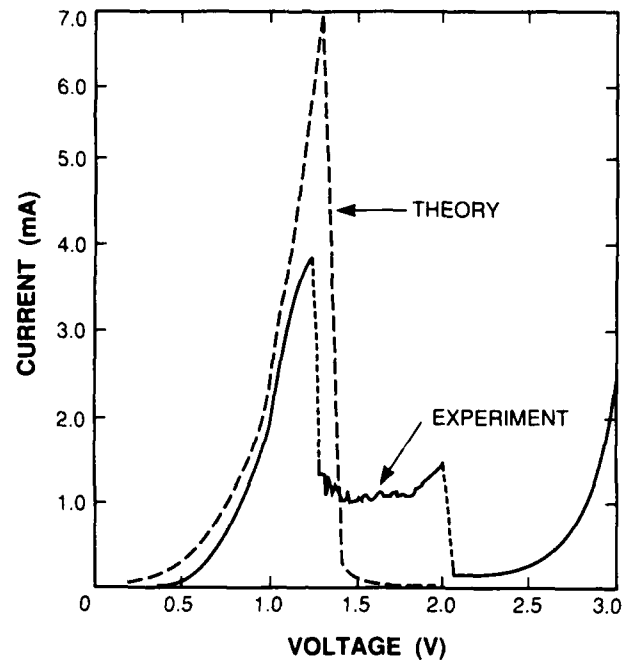*Figure 5-8. Room-temperature current-voltage curves for an 8-μm-diam. diode. The chairlike structure in the negative-resistance region is caused by self-detection of oscillations.*
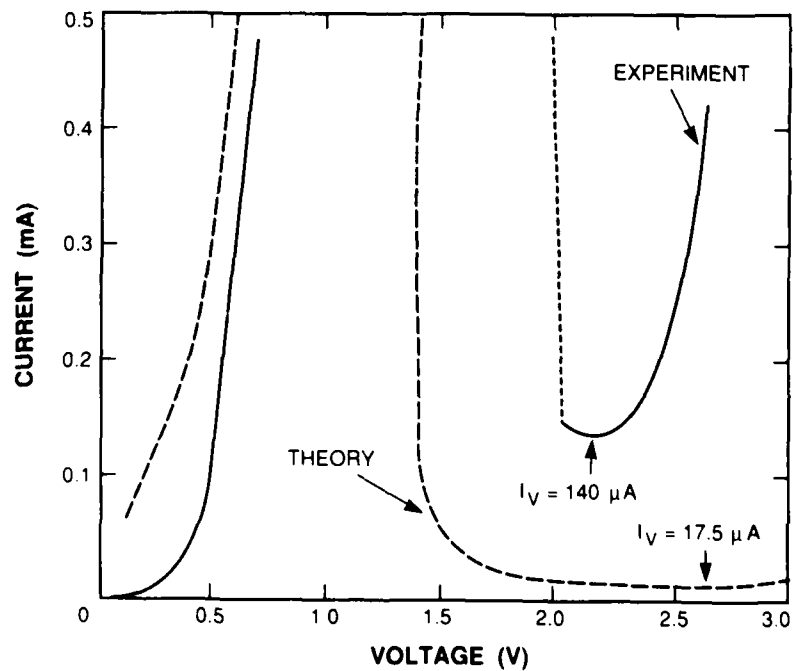
Figure 5-9. Room-temperature current-voltage curves with expanded vertical scale to show the relative size of the experimental (140 μA) and theoretical (17.5 μA) valley currents.

52

Figure 5-10.   Oscillation power data for an 8-μm-diam. device at room temperature. P_{MAX} is the maximum power and f_{MAX} is the maximum oscillation frequency, both derived from the RC model shown in the inset, with the following values: $G = -26$ mS, $R_S = 25$ Ω, and $C = 77$ fF.

112816-37

6. ANALOG DEVICE TECHNOLOGY
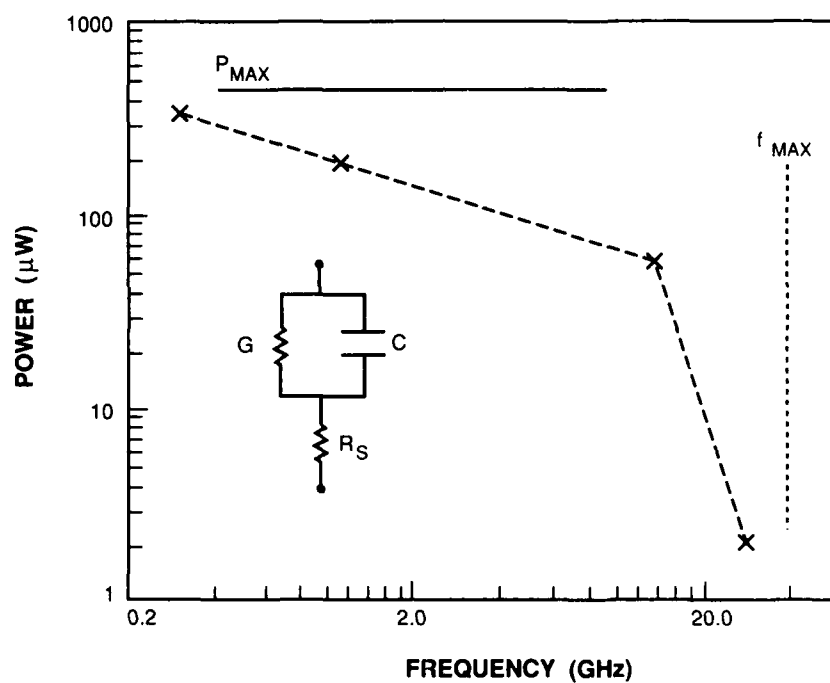
6.1 SUPERCONDUCTIVE Nb THIN-FILM CAPACITORS WITH Ta_2O_5 DIELECTRIC

A fabrication process for all-Nb thin-film capacitors with loss factor tan $\delta < 0.002$ at 1 MHz has been reported previously.[1] These capacitors are incorporated in the LC resonator circuit of the time-integrating correlator currently under development.[2]

During this quarter, a significant reduction in the capacitor loss due to its shunt conductance has been achieved by replacing the Nb_2O_5 dielectric with Ta_2O_5. The capacitors were fabricated by coating the Nb base electrode with a 30-nm-thick Ta film. The Ta deposition was carried out by RF diode sputtering immediately following the Nb deposition. The Ta deposition rate was 13 nm/min. The dielectric film was formed by anodizing the Ta film in an aqueous solution of ethylene glycol and ammonium pentaborate, with an oxide formation rate of 1.6 nm/V. The Ta_2O_5 thickness was in the range of 48 to 80 nm and varied by less than 0.3 nm over the 5-cm-diam. substrate. This uniformity is a necessary requirement to meet the close tolerances in the capacitor value (± 0.1 percent) in all the channels over an approximately 8-cm^2 device area. The relative dielectric constant (at 1 MHz) and the dielectric strength of the Ta_2O_5 formed by this process were 22 and 5×10^5 V/cm, respectively.

LC resonators fabricated with this process have Q's exceeding 1500 in the frequency range of 10 to 20 MHz. The improvement in Q values from 400 with Nb_2O_5 dielectric to 1500 with Ta_2O_5 dielectric will allow us to increase the resonant frequencies for a constant integration time. This translates into smaller area capacitors, enabling us to increase the circuit density for the next-generation (128-channel) correlator.

The modified process still uses all-refractory materials which can withstand repeated thermal cycling. Furthermore, the properties of the capacitors are insensitive to the conditions of the Nb counterelectrode sputtering; the high-pressure, low-power sputtering that must be used to avoid damaging the Nb_2O_5 dielectrics[1] and which provides counterelectrodes of inferior quality is not necessary. The Nb counterelectrode properties are hence readily compatible with the requirements of other devices in the circuit, such as Josephson junctions.

M. Bhushan

6.2 DEPOSITION OF $YBa_2Cu_3O_x$ FILMS BY SEQUENTIAL RF DIODE SPUTTERING

Superconducting thin films of $YBa_2Cu_3O_x$ have been prepared by annealing multilayer films deposited by sequential RF diode sputtering of Y_2O_3, BaF_2, and CuO targets. These three compounds have been selected as target materials because they are chemically stable in air. Since Ba and BaO readily react with atmospheric water, special care would be required for their use in our sputtering system, which is not vacuum loadlocked.

Figure 6-1 is a schematic of the sputtering system. A single RF source is connected to all three targets through separate tuning networks. The motion of the substrate table is controlled by a computer.
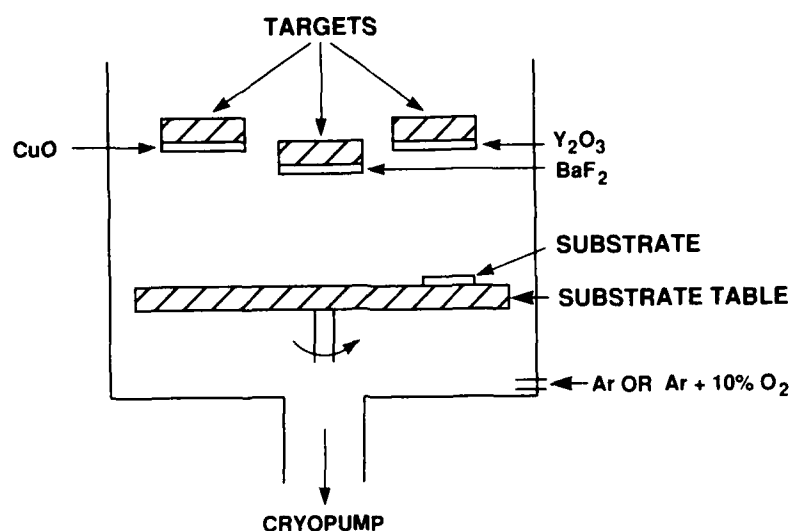
Figure 6-1. Schematic of the RF diode sputtering system.

The compositions and deposition rates of films obtained by sputtering each target have been measured as functions of RF power, sputtering gas composition (Ar or Ar + 10% O_2), gas pressure, target-to-substrate distance, and substrate temperature. The as-deposited Y_2O_3 films are stoichiometric. Sputtering the CuO target in Ar yields a mixture of CuO and Cu_2O, while sputtering in Ar + 10% O_2 yields single-phase CuO.

Sputtering the BaF_2 target produces BaF_2 films containing varying amounts of oxygen, depending on the partial pressure of oxygen. Optical emission spectroscopy of the plasma indicates the presence of Ba atoms and Ba^+ ions, but no F or F^- emission lines are detected. The Ba^+ ions are attracted to the target, which has a high negative potential. Formation of Ba^+ ions combined with possible electron and F^- ion bombardment of the substrate results in a reduced deposition rate. This effect has been observed in the sputter deposition of other Ba compounds as well.[3] The sputtering parameters for BaF_2 have been optimized to minimize Ba^+-ion production in order to achieve deposition rates of 20 to 30 nm/min.

In order to control the stoichiometry of the $YBa_2Cu_3O_x$ films, it is necessary to control the thickness of the individual as-deposited layers. The deposition rates vary during a run because of fluctuations in the power distribution among the three targets. Since the sputtering system cannot accommodate crystal deposition rate monitors, a new techique has been established to compute the film thickness during deposition. In an RF diode sputtering system, the target sputtering rate R is given by

$$R = KV^2$$

where V is the dc self-bias voltage of the target, and K is a constant for the target material and the geometry of the system.[4] Values of the constant K have been determined for each target

56

material for a fixed set of sputtering conditions. During a run, the target voltage is measured every 2 s and the film thickness is calculated by the computer, which moves the substrate table to position the substrate under the next target when the preset thickness is reached.

When no substrate heater is employed, the substrate temperature reaches 300° to 350°C during deposition as a result of ion and electron bombardment. The as-deposited films, containing 30 to 45 layers, are annealed in wet oxygen at 800° to 900°C for 30 min to remove the fluorine and then in dry oxygen to complete the formation of $YBa_2Cu_3O_x$.

Figure 6-2 is the resistance-vs-temperature plot for a $YBa_2Cu_3O_x$ film deposited on an yttria-stabilized ZrO_2 (YSZ) substrate and annealed at 850°C for 60 min. The onset of superconductivity occurs at 95 K, with zero resistance at 90 K. The film is 0.9 μm thick and has a resistivity of 1.7 mΩ-cm at 293 K. Figure 6-3 is an Auger depth profile of an annealed $YBa_2Cu_3O_x$ film on a YSZ substrate. The composition is close to the desired stoichiometry and is uniform through the film thickness. X-ray diffraction data show that all the $YBa_2Cu_3O_x$ films on YSZ are polycrystalline with no preferred orientation.

The surface roughness decreases as the individual as-deposited layers are reduced in thickness. Another factor affecting the surface roughness is the annealing temperature-time schedule. Annealing at 800°C for 5 h in oxygen has given the best results so far.
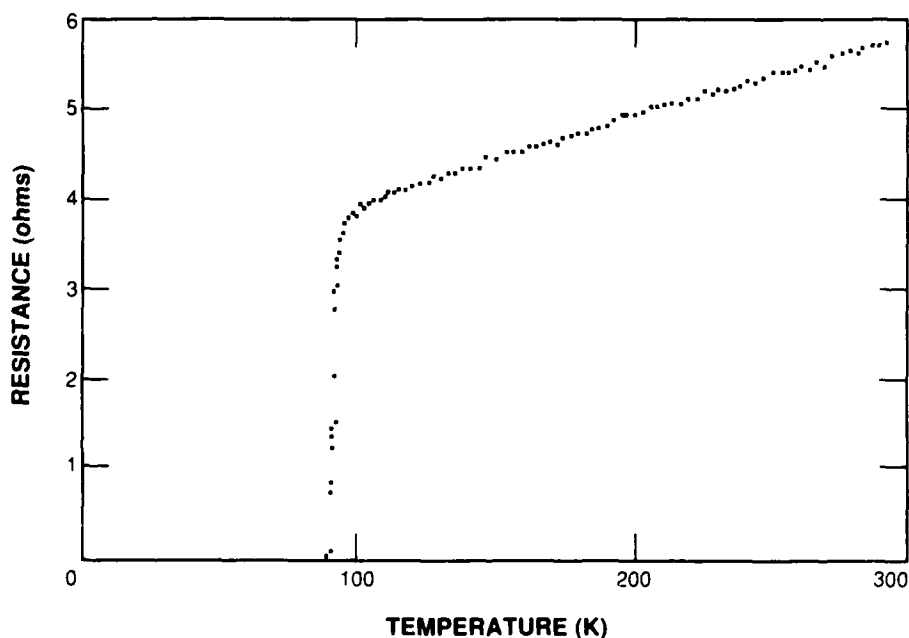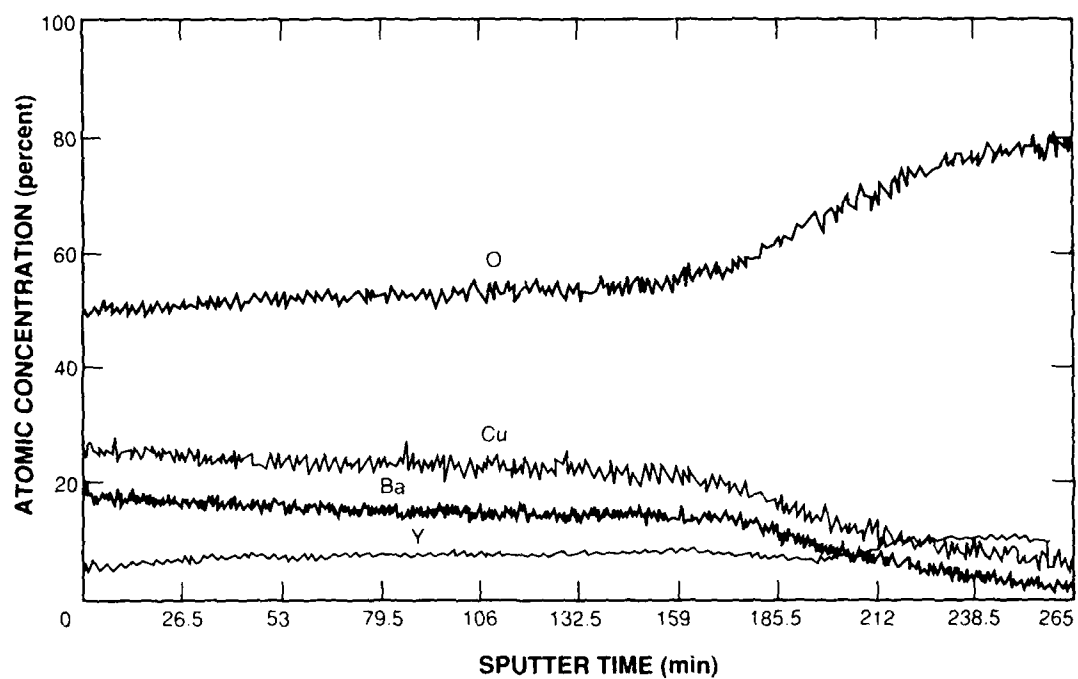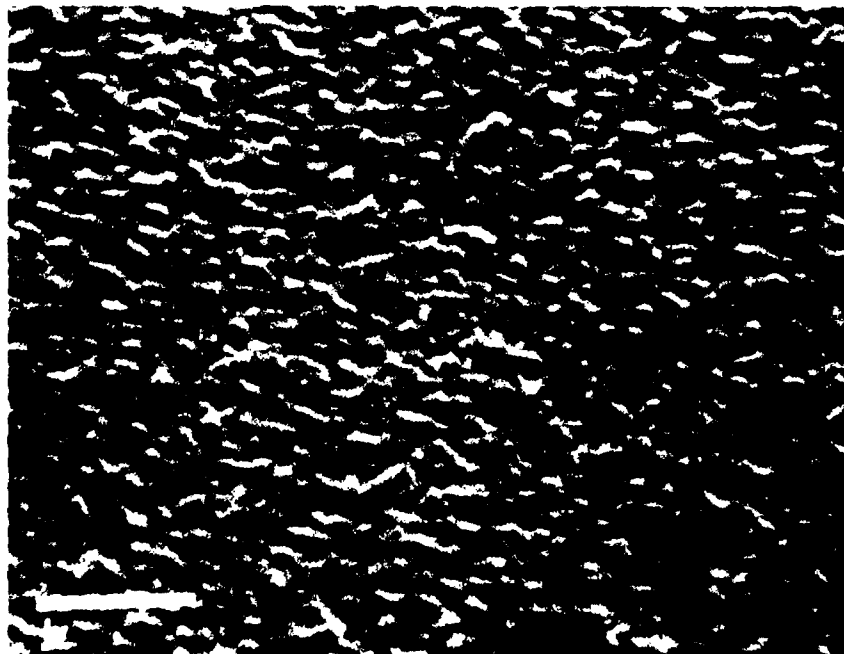

Figure 6-2.   Resistance-vs-temperature plot of a $YBa_2Cu_3O_x$ film deposited on yttria-stabilized ZrO_2 substrate.

57

Figure 6-3. *Auger depth profile of a* $YBa_2Cu_3O_x$ *film on an yttria-stabilized* ZrO_2 *substrate.*

Figure 6-4. *Scanning electron micrograph of a* $YBa_2Cu_3O_x$ *film on YSZ, annealed at 850°C for 60 min in* $O_2 + H_2O$ *followed by dry* O_2.

58

Figure 6-4 is a scanning electron micrograph of $YBa_2Cu_3O_x$ film, again on YSZ and annealed at 850°C for 60 min. The average grain size is less than 1 μm, and the film surface is smooth. These films are now being patterned using standard photolithographic techniques.

M. Bhushan
A.J. Strauss
M.C. Finn

6.3 MICROWAVE SURFACE RESISTANCE OF BiSrCaCuO FILMS

The discovery of materials that are superconducting above 77 K has rekindled worldwide interest in superconductivity. The high transition temperature of copper oxide materials such as yttrium-barium-copper oxide (YBCO) and bismuth-strontium-calcium-copper-oxide (BSCCO) has the potential for making space-based superconducting electronics practical. The usefulness of the new copper oxides in many applications will be determined by the surface impedance of these materials.

We have measured the surface resistance R_s of a BSCCO thin film in the frequency range 500 MHz $<$ f $<$ 10 GHz using a stripline-resonator technique described previously to measure the R_s of YBCO.[5]

The measured BSCCO film was deposited on a MgO substrate by magnetron cosputtering from separate Bi, Cu, and SrCa metal targets. After deposition, the film was annealed in O_2 at 890°C for 15 min. The film was 2500 Å thick and had a stoichiometry near $Bi_2Sr_2Ca_1Cu_2O_8$. The zero-resistance transition temperature for the film was ~65 K.

The results of our R_s measurements on the BSCCO film are shown in Figure 6-5 and are compared with our previous results for YBCO and those of other researchers using various techniques. The measured R_s for BSCCO at 4.2 K increases from ~10^{-3} $\Omega/\square$ at 500 MHz to 10^{-1} $\Omega/\square$ at 10 GHz.

The R_s of our BSCCO film increases as f^2, as would be expected of a superconducting material at frequencies well below that corresponding to its energy gap. The large magnitude of the R_s for BSCCO compared with the R_s of an elemental superconductor such as Nb may be attributed to several factors. First, the BSCCO film thickness may be smaller than the penetration depth of the film, which will add to losses. Second, the polycrystalline nature of the film will add the effects of grain boundaries and, hence, increase loss.[6] Finally, the film stoichiometry may not be uniform so that the entire film may not be superconducting. These factors would increase the losses in the resonator, resulting in the inference of a large R_s for the equivalent uniform film.

In spite of the additional losses due to these effects, the measured BSCCO film still had a lower R_s than Cu and Au up to 1 GHz. Above 1 GHz, however, the R_s of the BSCCO film rapidly becomes much larger than the corresponding values for both Au and Cu because of the f^2 dependence of R_s.
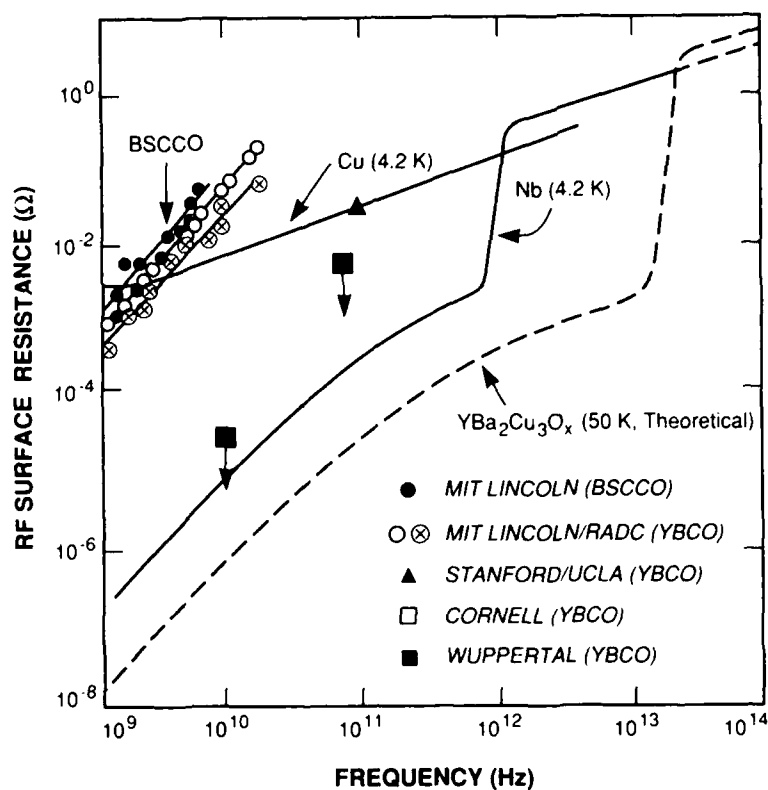
Figure 6-5. RF surface resistance of a thin film of BSCCO (shown at upper left) compared with previous results for YBCO polycrystalline thin films (MIT Lincoln/RADC), single-crystal bulk samples (Cornell), and epitaxial films (Stanford/ UCLA, Wuppertal). The arrows on the Cornell and Wuppertal data indicate that the values shown are upper bounds. Also shown for reference are the RF surface resistances of Cu and Nb at 4.2 K, and the theoretical resistance of YBCO at 50 K.

Our films suffer at present by being both nonuniform and polycrystalline. Our R_s measurements clearly indicate that these issues must be resolved before the superconducting copper oxides will be useful for large-scale electronics applications.

J.W. Steinbeck*
D.W. Face[†]
A.C. Anderson

---

* Rome Air Development Center

[†] MIT Center for Materials Science and Engineering

REFERENCES

1. Solid State Research Report, Lincoln Laboratory, MIT (1988:3), pp. 73-74.

2. *Ibid.* (1986:2), p. 59, DTIC AD-A180799.

3. S.I. Shah and P.F. Carcia, Appl. Phys. Lett. **51**, 2146 (1987).

4. L.T. Lamont, Jr. and F.T. Turner, J. Vac. Sci. Technol. **11**, 47 (1974).

5. Solid State Research Report, Lincoln Laboratory, MIT (1987:4), DTIC AD-A194708; M.S. DiIorio, A.C. Anderson, and B-Y. Tsaur, Phys. Rev. B **38**, 7019 (1988).

6. T.L. Hylton, A. Kapitulnik, M.R. Beasley, J.P. Carini, L. Drabeck, and G. Gruner, Appl. Phys. Lett. **53**, 1343 (1988).